The Astrophysical Journal, 909:60 (19pp), 2021 March 1 https://doi.org/10.3847/1538-4357/abd6ef

Dissecting the Supercritical Filaments Embedded in the 0.5 pc Subsonic Region of Barnard 5

Anika Schmiedeke[1], Jaime E. Pineda[1], Paola Caselli[1], Héctor G. Arce[2], Gary A. Fuller[3,4], Alyssa A. Goodman[5], María José Maureira[1], Stella S. R. Offner[6], Dominique Segura-Cox[1], and Daniel Seifried[7]
[1] Max-Planck-Institut für extraterrestrische Physik, Gießenbachstraße 1, D-85748 Garching, Germany; schmiedeke@mpe.mpg.de
[2] Department of Astronomy, Yale University, P.O. Box 208101, New Haven, CT 06520-8101, USA
[3] Jodrell Bank Centre for Astrophysics, Department of Physics and Astronomy, The University of Manchester, Oxford Road, Manchester M13 9PL, UK
[4] Intituto de Astrofísica de Andalucia (CSIC), Glorieta de al Astronomia s/n, E-18008 Granada, Spain
[5] Center for Astrophysics, Harvard & Smithsonian, 60 Garden Street, Cambridge, MA 02138, USA
[6] Department of Astronomy, The University of Texas at Austin, Austin, TX 78712, USA
[7] Universität zu Köln, I. Physikalisches Institut, Zülpicher Str. 77, D-50937 Köln, Germany
Received 2020 September 28; revised 2020 December 13; accepted 2020 December 27; published 2021 March 4

Abstract

We characterize in detail the two ∼0.3 pc long filamentary structures found within the subsonic region of Barnard 5. We use combined Robert C. Byrd Green Bank Telescope and Very Large Array observations of the molecular lines NH_3(1,1) and (2,2) at a resolution of 1800 au, as well as James Clerk Maxwell Telescope continuum observations at 850 and 450 μm at a resolution of 4400 and 3000 au, respectively. We find that both filaments are highly supercritical with a mean mass per unit length, M/L, of $\sim 80\,M_\odot\,\mathrm{pc}^{-1}$ after background subtraction, with local increases reaching values of $\sim 150\,M_\odot\,\mathrm{pc}^{-1}$. This would require a magnetic field strength of ∼500 μG to be stable against radial collapse. We extract equidistant cuts perpendicular to the spine of the filament and fit a modified Plummer profile as well as a Gaussian to each of the cuts. The filament widths (deconvolved FWHM) range between 6500 and 7000 au (∼0.03 pc) along the filaments. This equals ∼twice the radius of the flat inner region. We find an anticorrelation between the central density and this flattening radius, suggestive of contraction. Further, we also find a strong correlation between the power-law exponent at large radii and the flattening radius. We note that the measurements of these three parameters fall in a plane and derive their empirical relation. Our high-resolution observations provide direct constraints on the distribution of the dense gas within supercritical filaments showing pre- and protostellar activity.

Unified Astronomy Thesaurus concepts: Interstellar filaments (842); Star formation (1569); Star forming regions (1565)

1. Introduction

Dense cores are the places where stars form (see reviews by Bergin & Tafalla 2007; di Francesco et al. 2007; Ward-Thompson et al. 2007). They present nonthermal subsonic velocity dispersions (Fuller & Myers 1992; Goodman et al. 1998; Caselli et al. 2002) and represent the end of the turbulent cascade (Larson 1981).

One of the most popular molecular tracers to study the dense gas within and around dense cores is ammonia, NH_3. This is because the NH_3(1,1) transition traces material with densities starting at a few $10^3\,\mathrm{cm}^{-3}$. Also, due to its hyperfine structure, it is a useful determinant of optical depth and kinematic properties. In addition, the inversion transitions NH_3(1,1) and NH_3(2,2) usually can be observed simultaneously, as they are only separated by 28.1 MHz. The observation of these two transitions provides measurements of temperatures and column density (Friesen et al. 2017).

By mapping dense cores in NH_3(1,1), it was found that they show an almost constant level of nonthermal motion within a certain "coherence" zone (Goodman et al. 1998). The term "coherent core" describes the dense gas where nonthermal motions are roughly constant and typically smaller than thermal motions, independent of scale (see also Caselli et al. 2002).

Wide-field dust continuum observations with the Herschel Space Observatory have revealed that filaments are commonplace throughout molecular clouds, with lengths ranging from 0.5 pc up to several tens of parsecs. It was also established that they host most of the dense cores, with bound ones located predominantly in filaments with transcritical to supercritical masses per unit length (e.g., André et al. 2014; Arzoumanian et al. 2018, 2019). From these dust continuum observations, it is argued that the width of those filaments is close to 0.1 pc (Arzoumanian et al. 2011, 2019).

Studies using molecular line observations have also identified filamentary structures. Since molecular lines provide kinematic information, the filamentary structures are sometimes also analyzed by taking into account their coherence in velocity. Identified filaments using molecular lines usually have smaller lengths than those filaments seen by Herschel. A single several parsec long filament identified with Herschel can show several (in a few cases intertwined; Hacar et al. 2013; Henshaw et al. 2013) velocity-coherent filamentary structures when studied through molecular lines (Fernández-López et al. 2014; Hacar et al. 2017; Suri et al. 2019; Chen et al. 2020). Suri et al. (2019) found that the filament widths in the Orion A molecular cloud vary between 0.02 and 0.3 pc using $C^{18}O$(1–0), while filaments as narrow as 0.01 pc have been found in the OMC1 region using NH_3(1,1) observations (Monsch et al. 2018). Regarding their stability, the velocity-coherent structures or "fibers" in Hacar et al. (2013, 2017) were shown to have masses per unit length close to or below the stability value. Similar smaller-scale filaments were also identified within the coherent subsonic

region of Barnard 5 (hereafter B5; Pineda et al. 2011). At least one of the narrower filaments found in B5 displays an average radial profile that is different than those derived for the Herschel filaments.

Although efforts have been made to study the fragmentation of the filaments from the theoretical (e.g., Fiege & Pudritz 2000a; Hanawa et al. 2017, 2019) and the numerical side (e.g., Smith et al. 2014, 2016; Tomisaka 2014; Kirk et al. 2015; Seifried & Walch 2015; Clarke et al. 2019; Heigl et al. 2020), observational efforts have been focused on the fragments themselves (e.g., Pineda et al. 2015; Kainulainen et al. 2016), and an observationally driven understanding of filament fragmentation has yet to be established. The analysis of observations is usually performed on the average density profile. Hence, it is unclear if and how the density profile and width of a filament that is undergoing fragmentation change along the spine of the filament (i.e., its main axis). A robust observational determination of these properties along the spine of a filament would provide a strong constraint on theories of filament formation and evolution.

In this work, we focus on a region located in the Perseus star-forming region at a distance of (302 ± 21) pc from the Sun (Zucker et al. 2018). This region, called B5, has a nearly constant subsonic nonthermal velocity dispersion covering an area of $\sim 0.4\,\mathrm{pc} \times 0.6\,\mathrm{pc}$ and hosts at least one young stellar object (YSO), B5-IRS1 (Fuller et al. 1991). High angular resolution (6″, 1800 au) NH_3 observation reveals filamentary substructures within the subsonic region (Pineda et al. 2011). Embedded in these filaments are, in addition to the already-mentioned YSO, three gravitationally bound dense gas condensations (Pineda et al. 2015) forming a wide-separation quadruple system. This quadruple system appears to be the result of fragmentation of the dense gas filaments. Here we use these high angular resolution, high-density tracer observations of NH_3 to study in detail the density profile of the filamentary structure embedded in the coherent zone of B5.

The paper is structured as follows. In Section 2, we present the observational data used in this paper. In Section 3, we report the results of the analysis of the filamentary structure. These results are discussed in Section 4. We conclude the paper in Section 5.

2. Observations

We use observational data from three different telescopes: continuum maps at 450 and 850 μm obtained with the James Clerk Maxwell Telescope (JCMT) and combined observations of two metastable ammonia transitions, $NH_3(1,1)$ and (2,2), obtained with the Robert C. Byrd Green Bank Telescope (GBT) and the Very Large Array (VLA). These observational data have already been published (Pineda et al. 2015). For clarity, we briefly list the important details of these observations.

2.1. JCMT

Observations at 450 and 850 μm of the B5 cloud were performed using the Submillimetre Common-Use Bolometer Array 2 (SCUBA-2; Holland et al. 2013) at the JCMT (project code M13BU14) during grade 1 weather. The 450 and 850 μm observations were carried out simultaneously on 2013 August 16 and 23 and September 3. The iterative mapmaking technique was used with the command `makemap` (Chapin et al. 2013) of the Starlink software suite,[8] with a pixel size of 0.″5 to match the $NH_3(1,1)$ VLA map (see Section 2.2). Details of the data reduction can be found in Pineda et al. (2015). The maps have a spatial resolution of 9.″8 (3000 au) at 450 μm and 14.″6 (4400 au) at 850 μm. The noise level in the emission-free regions is 0.23 mJy pixel^{-1} at 450 μm and 0.026 mJy pixel^{-1} at 850 μm.

2.2. GBT and VLA

The GBT observations of the B5 region were carried out between 2009 December 23 and 2010 March 21 (project number 08C-088). Two 12.5 MHz windows were centered on $NH_3(1,1)$ and $NH_3(2,2)$ and observed in frequency-switching mode. The spectral resolution of the data is 0.04 km s^{-1}. Details of the data processing can be found in Pineda et al. (2010).

The single-dish GBT data were combined with high-resolution interferometric data obtained with the VLA. The VLA observations were carried out in the D-array configuration on 2011 October 16–17 and in the DnC-array configuration on 2012 January 13–14 (project number 11B-101). The WIDAR correlator was configured such that two basebands with 4 MHz bandwidth were centered on $NH_3(1,1)$ and $NH_3(2,2)$, with a spectral resolution of 0.049 km s^{-1}. Detailed information on the data processing can be found in Pineda et al. (2015). The spatial resolution of the final map is 6.″0 (1800 au).

3. Results

3.1. Morphology of the Subsonic Region in B5

The substructure of the B5 coherent region is more easily identified in the high-contrast NH_3 integrated intensity image than in the Herschel images, since NH_3 does not trace the more extended structure seen in the Herschel dust continuum emission due to NH_3 either not being present or having very low abundance.

We characterize the morphology of the coherent region employing `astrodendro` (Rosolowsky et al. 2008) on the $NH_3(1,1)$ integrated intensity map. By using a clipping method, `astrodendro` assigns emission above a certain threshold (contour level) as associated with an object. We provide the minimum value to be considered in the map (0.03 Jy beam^{-1} km s^{-1}, i.e., 10 times the rms), the height threshold value that determines if a leaf will be a single entity or not (0.01 Jy beam^{-1} km s^{-1}), and a minimum number of pixels for a leaf to be considered a single entity (250 pixels). Figure 1 shows the identified substructure with different contours.

Two independent clumps are identified: B5-clump1 and B5-clump2. While B5-clump1 appears smooth and without signs of active star formation (quiescent), B5-clump2 breaks up further and shows clear signs of fragmentation. We identify two independent filamentary structures: B5-fil1 and B5-fil2. Along the spines of both filamentary structures, we identify three leaves representing three gas condensations: B5-cond1, B5-cond2, and B5-cond3. This finding is in agreement with Pineda et al. (2015), in which the three condensations along with the protostellar source B5-IRS1 were found to be bound and on their way to form a wide-separation quadruple system. Furthermore, here we identify lower-level overdensities along both filament spines, which might provide the seeds for future

[8] http://starlink.eao.hawaii.edu/starlink

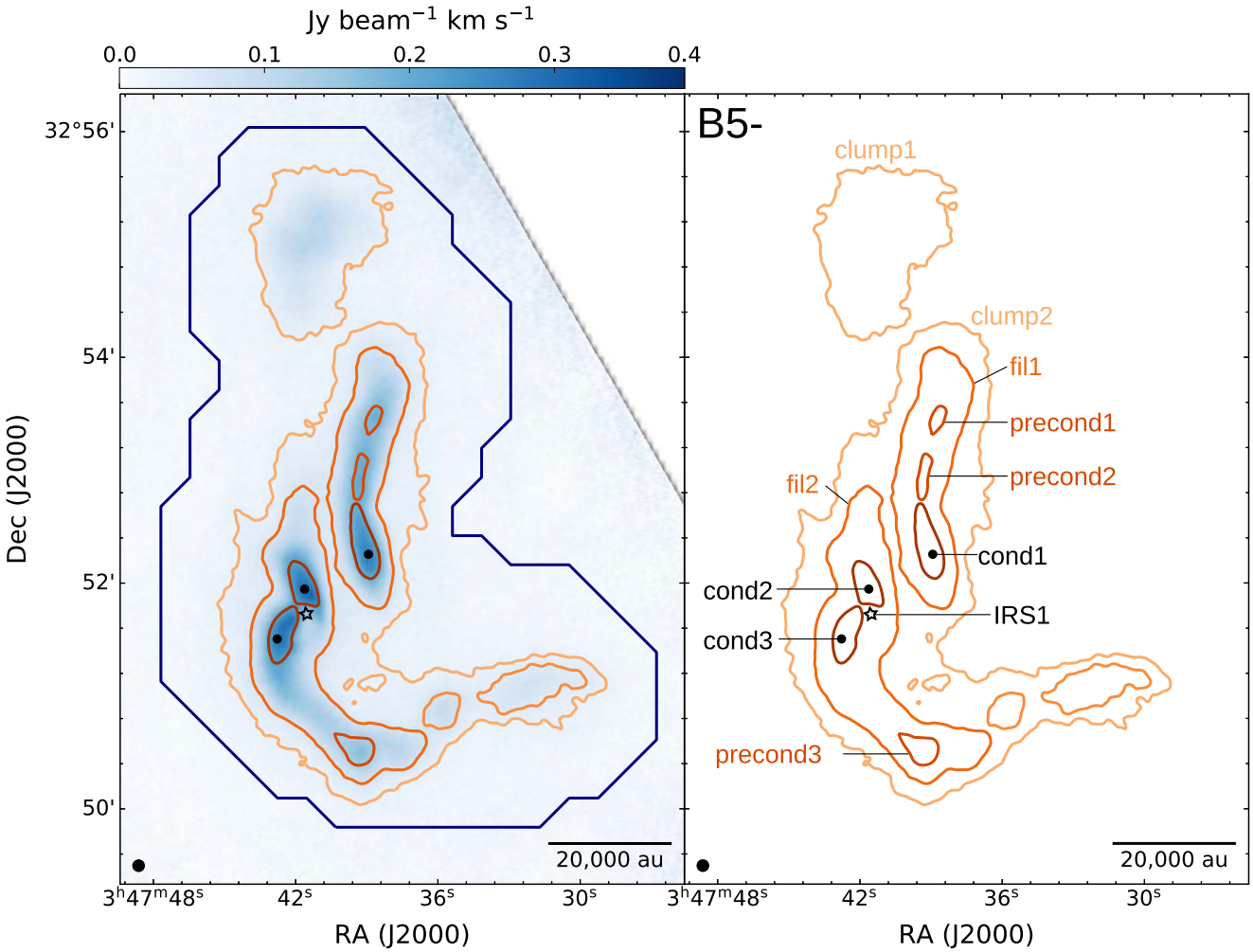

Figure 1. In the left panel, the integrated intensity map of VLA and GBT combined $NH_3(1,1)$ is shown in the background. The navy contour indicates the extent of the coherent zone (Pineda et al. 2010). Right: boundaries and nomenclature for the regions used in this work. The yellow, orange, and red contours indicate the structures identified using dendrograms. The black star and circles mark the locations of the protostar B5-IRS1 and the gas condensations, respectively (Pineda et al. 2015). The beam and scale bar are shown in the bottom left and right corner, respectively.

fragmentation (precondensations). The peak intensities of these precondensations are about 25% lower than the faintest condensation.

3.1.1. General Properties of the Substructures

We simultaneously fit the $NH_3(1,1)$ and $NH_3(2,2)$ data cubes using `pySpecKit` (Ginsburg & Mirocha 2011) to obtain information on the NH_3 column density, the kinetic temperature, and the velocity field. Details of this fitting procedure are given in Appendix A. The resulting property maps are shown in Figure 2.

For each substructure, we list the mean properties obtained from the `pySpecKit` fitting in Table 1. This includes the NH_3 column density, kinetic temperature, line-of-sight velocity, and nonthermal velocity dispersion. The nonthermal velocity dispersion σ_{nt} is calculated from the fitted velocity dispersion σ_v as

$$\sigma_{nt} = \sqrt{\sigma_v^2 - \sigma_{th}^2}, \quad (1)$$

where σ_{th} is the thermal velocity dispersion.

We notice that the filaments have a lower mean kinetic temperature compared to the clumps. It is also interesting to note that B5-cond1, which is embedded in B5-fil1, has a mean kinetic temperature of 8.5 K, while the other two condensations, B5-cond2 and B5-cond3, have higher mean kinetic temperatures of 10.7 K. These two condensations are embedded in B5-fil2, relatively close to the YSO B5-IRS1, and likely affected by the stellar feedback. The line-of-sight velocities are comparable for all structures, suggestive of shallow velocity gradients along the line of sight within the coherent zone of B5. The nonthermal velocity dispersion is subsonic, as expected. The velocity dispersion map shows a subtle increase at the position of the condensations, and the centroid velocity map shows variations where the additional clumpy substructure appears.

3.2. Filamentary Structure

3.2.1. Filament Length and Profiles Perpendicular to Filament Spines

We employ the python-based package `radfil` (Zucker & Chen 2018) to further characterize both filamentary structures. Based on the provided $NH_3(1,1)$ intensity map and a mask,

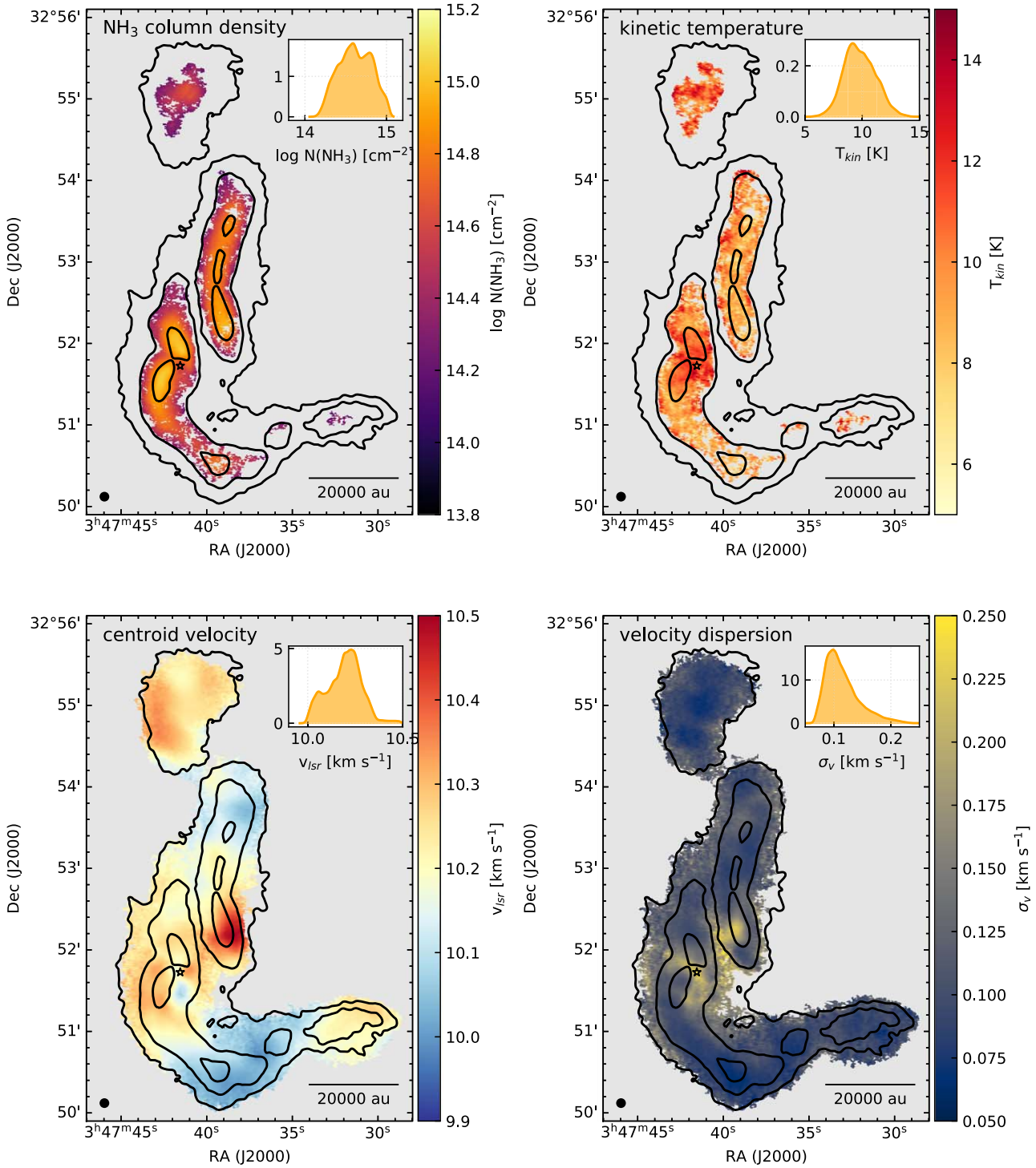

Figure 2. Fit results from simultaneous fitting of NH_3(1,1) and (2,2) using pySpecKit. Top left: NH_3 column density in logarithmic scale. Top right: kinetic temperature T_{kin}. Bottom left: centroid velocity v_{lsr}. Bottom right: velocity dispersion σ_v. The black contours are the same as in Figure 1. The inset in the top right corner of each panel shows the distribution of the respective parameter. The beam and scale bar are shown in the bottom left and right corner of each map, respectively. The black star marks the location of the protostar B5-IRS1. Details of the line fitting procedure are given in Appendix A.

radfil employs the package `fil_finder` (Koch & Rosolowsky 2015) to define the spines of the filaments. Following the spines of the filaments, we determine filament lengths of 0.24 and 0.31 pc for B5-fil1 and B5-fil2, respectively. Going along the filament spine, we extract equidistant cuts perpendicular to the spine using a sampling frequency of 12 pixels. This yields roughly a one-beam separation between individual cuts (6″ beam, 0.″5 pixel size). The resulting profiles are shifted such that the center coincides with the peak intensity. The spine and the perpendicular cuts are shown in Figure 3.

To investigate the filament properties, we follow the approach presented by Arzoumanian et al. (2011) and adopt

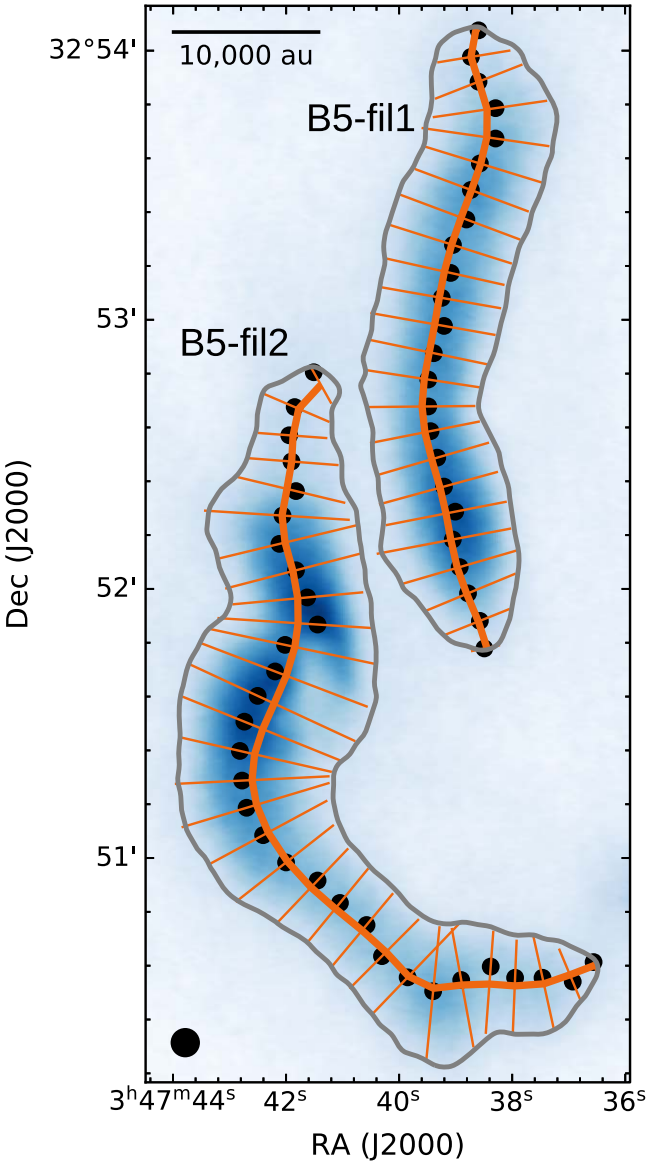

Figure 3. Ammonia integrated intensity map of the masked filaments. The spines of the filaments are marked by the thick orange lines. The perpendicular cuts are marked by the thin orange lines. The peak pixel of each intensity cut is indicated by a black circle. The beam is indicated by the black circle in the bottom left corner.

Table 1
Averaged Properties of the Substructure of the Coherent Region of B5, Shown in Figure 1

ID (B5-)	$\langle \log(N(NH_3)) \rangle$ (cm^{-2})	$\langle T_{kin} \rangle$ (K)	$\langle v_{lsr} \rangle$ (km s^{-1})	$\langle \sigma_{nt} \rangle$ (km s^{-1})
clump1	14.42 ± 0.12	10.7 ± 1.3	10.26 ± 0.05	0.06 ± 0.02
clump2	14.65 ± 0.20	9.7 ± 1.3	10.18 ± 0.09	0.09 ± 0.04
fil1	14.66 ± 0.18	9.2 ± 1.2	10.22 ± 0.11	0.10 ± 0.04
fil2	14.65 ± 0.19	9.9 ± 1.3	10.19 ± 0.09	0.09 ± 0.04
precond1	14.82 ± 0.03	8.4 ± 1.0	10.13 ± 0.01	0.08 ± 0.01
precond2	14.85 ± 0.02	8.5 ± 0.9	10.22 ± 0.01	0.08 ± 0.01
precond3	14.70 ± 0.05	8.3 ± 0.6	10.05 ± 0.03	0.04 ± 0.01
cond1	14.87 ± 0.05	8.6 ± 0.7	10.36 ± 0.08	0.14 ± 0.04
cond2	14.94 ± 0.06	10.8 ± 0.7	10.24 ± 0.03	0.12 ± 0.03
cond3	14.94 ± 0.06	10.6 ± 0.9	10.28 ± 0.03	0.11 ± 0.03

the idealized model of a cylindrical filament with a radial density $n(r)$ and column density $\Sigma(R)$ profile as

$$n(r) = \frac{n_0}{[1 + (r/R_{\rm flat})^2]^{p/2}} + n_{\rm bkg}$$
$$\longrightarrow \Sigma(R) = A_p \frac{\Sigma_0}{[1 + (R/R_{\rm flat})^2]^{\frac{p-1}{2}}} + \Sigma_{\rm bkg}, \quad (2)$$

where

$$\Sigma_0 = n_0 R_{\rm flat}. \quad (3)$$

Here r is the cylindrical radius from the spine of the filament, R is the projected radius, n_0 is the central density of the cylinder, $R_{\rm flat}$ is the radius of the flat inner section of the cylinder, $n_{\rm bkg}$ and $\Sigma_{\rm bkg}$ are the (constant) background density and surface density, respectively, and A_p is a finite constant factor that depends on the density profile power-law index p and the filament inclination angle (which we assume to be equal to zero for simplicity). For $p = 2$, the filament width is $W \sim 3R_{\rm flat}$ (Arzoumanian et al. 2011). But, more commonly, the filament width is defined as the FWHM of a Gaussian fit to the inner part of the cuts (e.g., Arzoumanian et al. 2011; Panopoulou et al. 2017). Hence, in addition to fitting a Plummer function, we also fit a Gaussian to the innermost (8000 au) part of the cut, taking into account the constant background emission,

$$g(R) = \frac{A_{\rm G}}{\sigma_{\rm G}\sqrt{2\pi}} \exp\left(-\frac{(R - \mu_{\rm G})^2}{2\sigma_{\rm G}^2}\right) + g_{\rm bkg}, \quad (4)$$

where $A_{\rm G}$ is the amplitude, $\sigma_{\rm G}$ is the variance, and $\mu_{\rm G}$ is the expected value. From this, the FWHM is calculated as $\mathrm{FWHM} = 2\sigma_{\rm G}\sqrt{2\ln 2}$. The beam is taken into account by deconvolving the FWHM following Könyves et al. (2015), i.e., the deconvolved FWHM, $\mathrm{FWHM_d} = \sqrt{(\mathrm{FWHM}^2 - \mathrm{HPBW}^2)}$, where HPBW is the half-power beamwidth in au. For our observations, the HPBW is 6″, corresponding to ~1800 au at the distance of B5. For the Plummer fits, we convolve the Plummer-like function with the 6″ Gaussian beam prior to fitting.

To investigate the global properties of the filaments, we first fit the average profiles of each filament. In Figure 4, we show the average profiles with black solid lines. The individual profiles are superimposed in light gray. When fitting the profiles, we restrict the fitting range to avoid contamination from peak structures from the other filament. The background emission is determined by fitting a constant to the flat outer edges of the profile cuts. We fit three different versions of Equation (2): (i) the exponent is fixed to 2, (ii) the exponent is kept as a free parameter, and (iii) the exponent is fixed to 4. The latter is the Ostriker (1964) solution for an isothermal filament in hydrostatic equilibrium. The best fits of all three versions are shown in Figure 4 in gold, orange, and blue, respectively.

We list the fitting results in Table 3 in Appendix C (data set "NH_3, 6″"). We use the Akaike information criterion (AIC) to evaluate the goodness of the fits, where the model with the lowest AIC value is the preferred one. For both filaments, the

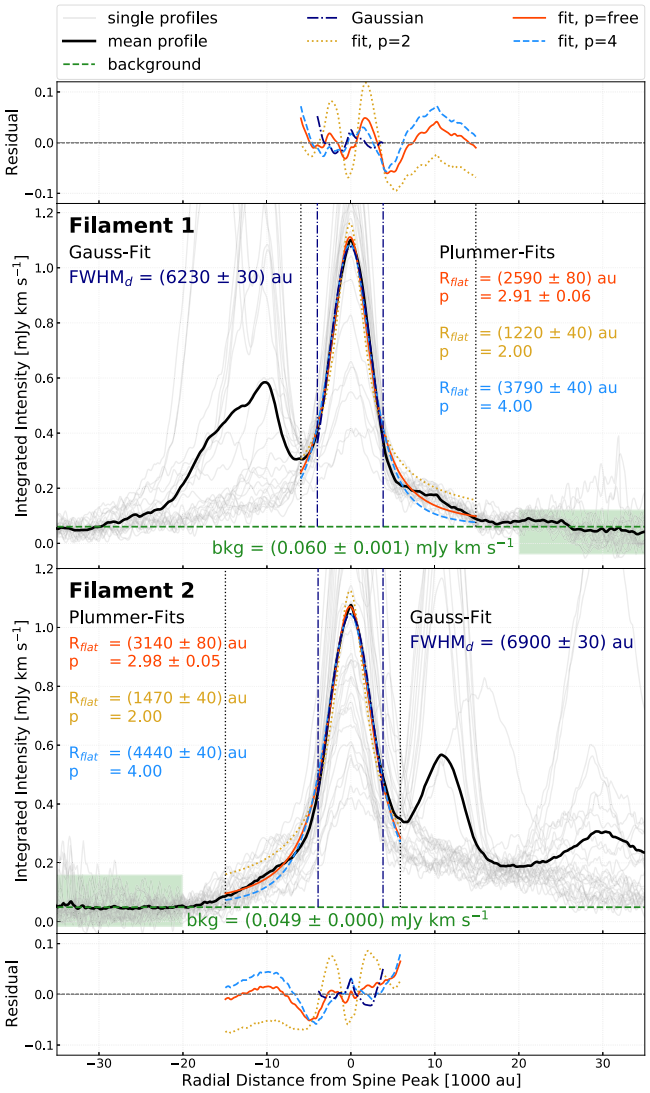

Figure 4. Results from fitting the average profiles (black solid lines) with a Gaussian profile (navy dashed–dotted line, which mostly overlaps with the averaged profile) and a Plummer profile, for which (i) the exponent is fixed to 2 (gold dotted line), (ii) the exponent is fixed to 4 (light blue dashed line), and (iii) the exponent is kept as a free parameter (orange solid line). Top: B5-fil1. Bottom: B5-fil2. The light gray lines are the individual profile cuts. The secondary peak in the average profile (on the left for B5-fil1 and on the right for B5-fil2) is the contamination of the profile cut from the respective other filament. This has been excluded from the fitting. The fitting range is indicated by the vertical navy dashed–dotted lines for the Gaussian fit and the vertical black dotted lines for the Plummer fits. The horizontal green dashed line indicates the background emission, obtained by fitting the outer edge of the profile cuts; only the uncontaminated side of the average profile is used for the background determination (marked with light green shading).

lowest AIC value is determined for the fit with a Plummer function where the exponent has been kept as a free parameter.

We then fit each individual perpendicular cut with a Gaussian and a Plummer-like profile, where the exponent is kept as a fitting parameter. From this fitting, we obtain the variation of the filament parameters (mass, central density, width, and exponent) as a function of location along the filament spines. These results are presented in detail in the following subsections.

3.2.2. Filament Mass

We follow two independent strategies to determine the mass of the filaments: (a) scaling the $NH_3(1,1)$ integrated emission using the JCMT 450 μm map and (b) converting the NH_3 column density to mass. A detailed description of the procedures and comparison of both conversions is given in Appendix B. In short, for method (a), we convert the JCMT 450 μm background-corrected[9] flux density in B5-cond1 to gas mass assuming a gas-to-dust ratio of 100 (Hildebrand 1983), a distance of 302 ± 21 pc (Zucker et al. 2018), a dust temperature of 9 ± 1 K (deduced from the kinetic temperature map and assuming that the dust temperature is coupled to the gas temperature), and optically thin dust with a dust absorption coefficient of $\kappa_{450\,\mu m} = 6.4 \pm 0.81\,\mathrm{cm^2\,g^{-1}}$ (Ossenkopf & Henning 1994). For the same condensation, B5-cond1, we measure the background-corrected (See footnote 9) flux density in the integrated $NH_3(1,1)$ map. This yields an ammonia-to-mass conversion factor of $(1.5 \pm 0.7)\,M_\odot\,\mathrm{Jy^{-1}}$. For method (b), we convert the ammonia column density derived from the `pySpecKit` fitting assuming an abundance of ammonia with respect to H_2 of $10^{-8.5}$ (Friesen et al. 2017). The resulting mass maps agree within a factor of 2 with each other (method (b) yields a factor of 2 higher mass compared to method (a)). The ratio of both maps is smooth and does not show any strong gradients. All mass-dependent calculations in this work will be performed on the basis of the mass map derived with the dust-scaling method (a), since it is a conservative estimate.

For the entire filaments B5-fil1 and B5-fil2, we measure background-corrected flux densities of 6.29 and 8.97 Jy, respectively, in the $NH_3(1,1)$ integrated intensity map. We determine the background as the pixel within the filament with the lowest flux density (~0.4 mJy for both filaments). This is very likely overestimating the real background; hence, it results in a very conservative mass determination. We obtain total background-corrected masses of $M_{\mathrm{B5\text{-}fil1}} = 9.4$ and $M_{\mathrm{B5\text{-}fil2}} = 13.4\,M_\odot$.

3.2.3. Filament Mass per Unit Length

We determine the mass per unit length, M/L, to be $39.2\,M_\odot\,\mathrm{pc^{-1}}$ for B5-fil1 and $43.2\,M_\odot\,\mathrm{pc^{-1}}$ for B5-fil2. We note that this is a conservative estimate due to the aggressive background determination.

A more realistic approach encompasses determining the local variation of filament mass. Here, for each cut perpendicular to the filament spine, the background is determined by fitting a constant to the outer edges of the cuts. The determined background values are 0.05–0.06 mJy. We subtract this background when calculating the mass enclosed in the filament cut. To obtain the mass per unit length, we divide the mass contained in the individual cut by the length of the cut in the direction of the filament spine. In panel (b) of Figure 5, we show the variation of filament background-corrected mass per unit length along the filament spine. The mean value is $74.2\,M_\odot\,\mathrm{pc^{-1}}$ for B5-fil1 and $83.3\,M_\odot\,\mathrm{pc^{-1}}$ for B5-fil2, which we also list in Table 2. Due to the ~one-beam separation between the cuts and the filaments being rather straight, the overlap of individual cuts and hence the duplication when determining the mass is minimal (see Figure 3).

The critical value $(M/L)_{\mathrm{crit}}$ for an isothermal cylinder of gas in hydrostatic equilibrium is (Ostriker 1964)

$$(M/L)_{\mathrm{crit}} = \frac{2c_s^2}{G} \sim 16.6\left(\frac{T_{\mathrm{gas}}}{10\ \mathrm{K}}\right) M_\odot\ \mathrm{pc^{-1}}, \quad (5)$$

[9] We determine the background as the pixel within the structure with the lowest value.

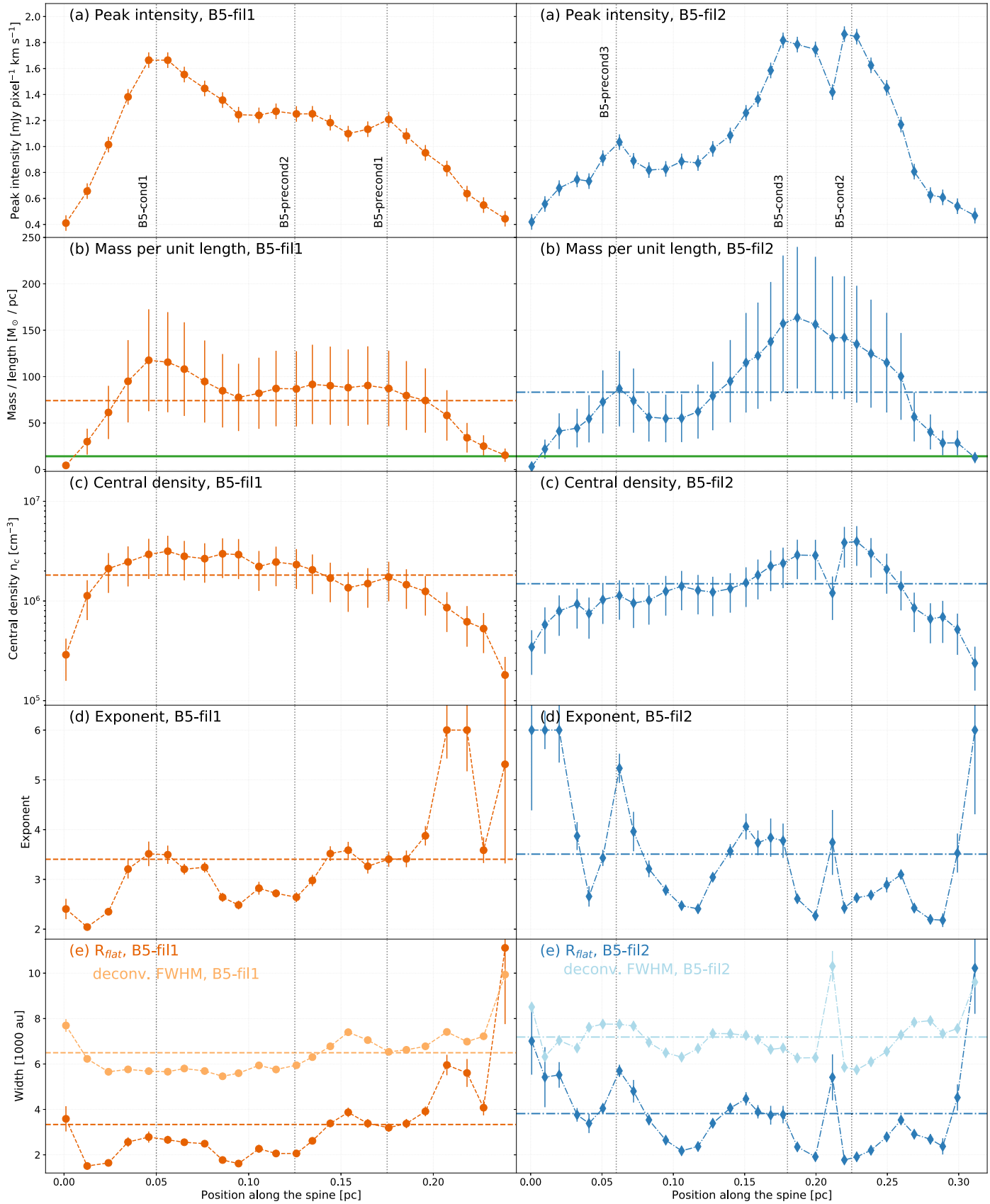

Figure 5. Properties along the spines of the filaments. Left: B5-fil1, marked with orange circles and a dashed line. Right: B5-fil2, marked with blue diamonds and a dashed–dotted line. (a) Spine peak intensity. (b) Mass per unit length; the solid green line indicates the critical limit determined by Ostriker (1964) for a 10 K cylinder with subsonic turbulence. (c) Central density. (d) Exponent p from Equation (2). (e) $R_{\rm flat}$ and deconvoled FWHM in lighter colors. The dashed and dashed–dotted horizontal lines mark the average values of the spine properties. The locations of the condensations and precondensations are marked by the vertical gray dotted lines and labeled in the top panel. The position 0.0 starts to the south of each spine.

Table 2
Derived Filament Properties

Parameter	B5-fil1	B5-fil2
Flux density F [Jy]		
$F_{\rm fil}$	11.95	17.50
$F_{\rm fil,bkg\text{-}sub}$	6.29	8.97
Mass M [$M_\odot$]		
$M_{\rm fil}$	17.9	26.1
$M_{\rm fil,bkg\text{-}sub}$	9.4	13.4
Length L [pc]	0.24	0.31
M/L [$M_\odot$ pc^{-1}]		
$(M/L)_{\rm fil}$	74.5	84.1
$(M/L)_{\rm fil,bkg\text{-}sub}$	39.2	43.2
$\overline{(M/L)}_{\rm cuts}$	80.6	88.0
$\overline{(ML)}_{\rm cuts,bkg\text{-}sub}$	74.2	83.3
Central density n_0 [10^6 cm^{-3}]		
$(n_0)_{\rm avgProfile}$	1.7	1.4
$\overline{(n_0)}_{\rm cuts}$	1.8	1.5
$R_{\rm flat}$ [au]		
$(R_{\rm flat})_{\rm avgProfile}$	2600	3100
$\overline{(R_{\rm flat})}_{\rm cuts}$	3300	3800
FWHM$_{\rm d}$ [au]		
$(\rm FWHM_d)_{\rm avgProfile}$	6200	6900
$\overline{(\rm FWHM_d)}_{\rm cuts}$	6500	7200
Exponent p		
$(p)_{\rm avgProfile}$	2.91	2.98
$\overline{(p)}_{\rm cuts}$	3.40	3.51
Kinetic temperature $T_{\rm kin}$ [K][a]	8.7	9.6
Velocity dispersion $\sigma_{\rm v,NH_3}$ [km s^{-1}][a]	0.117	0.104

Note.
[a] Average value along the spine of the filament.

where c_s is the sound speed of the gas, G is the gravitational constant, and $T_{\rm gas}$ is the gas temperature. Both filaments exceed this critical value by, on average, a factor of 3–4. Locally, this can even increase by factors of 5. Both filaments are supercritical, which means that their thermal pressure is insufficient to support them against gravitational collapse. They should collapse further unless there are means providing additional support (e.g., magnetic fields). This is discussed in Section 4.3.

3.2.4. Central Density

Similar to the determination of the flux-to-mass conversion factor ξ outlined in Section 3.2.2, we calculate a flux–to–column density factor Ξ as

$$\Xi = \frac{\mathcal{G}}{\kappa_\nu\, \mu_{\rm H_2}\, m_{\rm H}\, \Omega\, B_\nu(T_d)}, \tag{6}$$

where $\mathcal{G}$ is the gas-to-dust ratio ($\mathcal{G} = 100$; Hildebrand 1983), κ_ν is the dust absorption coefficient at the frequency ν, $\mu_{\rm H_2}$ is the molecular weight per hydrogen molecule ($\mu_{\rm H_2} = 2.8$; Kauffmann et al. 2008), $m_{\rm H}$ is the mass of the hydrogen atom, Ω is the area (in our case of B5-cond1), and $B_\nu(T_d)$ is the Planck function evaluated at the dust temperature T_d. We determine a 450 μm flux–to–column density factor of $\Xi = (4.4 \pm 1.9)10^{25}$ Jy^{-1} cm^{-2}. From the flux measured for B5-cond1 in both the JCMT 450 μm and the $NH_3(1,1)$ map, we determine an ammonia–to–column density conversion factor of $\eta = (1.25 \pm 0.53)\ 10^{26}$ Jy^{-1} cm^{-2}.

We fit the observed intensity profile of the cuts perpendicular to the filament spine with a modified Plummer function (similar to Equation (2); see Section 3.2.1), where the fitting parameter A is given as

$$A = \frac{n_0\, A_p\, R_{\rm flat}}{\eta}. \tag{7}$$

This allows us to determine the central density n_0. From the fit to the average profile of the filament cuts, we determine a central density of $(1.7 \pm 0.7)\ 10^6$ cm^{-3} for B5-fil1 and $(1.4 \pm 0.6)\ 10^6$ cm^{-3} for B5-fil2. In panel (c) of Figure 5, we show the variation of central density along the filament spines for both filaments, determined from the individual fits to the filament profiles. The mean of the central density derived from the individual fits is 1.8×10^6 cm^{-3} for B5-fil1 and 1.5×10^6 cm^{-3} for B5-fil2, just slightly higher compared to the value determined from fitting the average profile (see also Table 2). As expected, we see an increase in central density toward the location of all three condensations. We note that the profiles of the variation of central density along the filament spines visually appear to be similar when one flips one profile and aligns the condensations. This is further evaluated in Section 4.1. The central density, on the order of 10^6 cm^{-3}, is comparable to central densities found in prestellar cores like L1544 (Crapsi et al. 2005).

3.2.5. Filament Width and Exponent

From the Gaussian fit of the averaged profiles, we obtain a deconvolved FWHM$_{\rm d}$ of (6200 ± 30) au for B5-fil1 and (6900 ± 30) au for B5-fil2, which corresponds to $\sim 2R_{\rm flat}$ for the Plummer fits, where the exponent p has been kept as a free parameter. Given their lengths, we determine aspect ratios, i.e., length over FWHM$_{\rm d}$, of 17:1 and 10:1 for B5-fil1 and B5-fil2, respectively.

We then apply the same Gaussian fitting to each individual cut along the filament spines as described in Section 3.2.1. Panel (e) in Figure 5 shows the variation of $R_{\rm flat}$ and FWHM$_{\rm d}$ along the spines of both filaments. The mean of FWHM$_{\rm d}$ is 6500 au for B5-fil1 and 7200 au for B5-fil2 (see also Table 2). Both values agree well with the results from fitting the average profile. The deviation could be caused by the higher uncertainty in the fits due to the lower signal-to-noise ratio (S/N) toward the tips of the filaments. We discuss the determined filament widths further in Section 4.2.

The mean of $R_{\rm flat}$ is 3300 au for B5-fil1 and 3800 au for B5-fil2. Hence, the mean of $R_{\rm flat}$ increases by about 20%–30% when fitting the individual profiles as opposed to fitting the average profiles. This increase is likely linked to the increase in the exponent. Fitting the average profile with a Plummer profile where the exponent has been kept as a free parameter yields exponent values of $p \approx 3$. When fitting the individual profiles, we determine a mean value of $p \approx 3.5$. A value of $p = 4$ represents a special case of an isothermal filament in hydrostatic equilibrium (Ostriker 1964). Lower values of p, $1.5 < p < 2.5$, are typically found in molecular cloud filaments

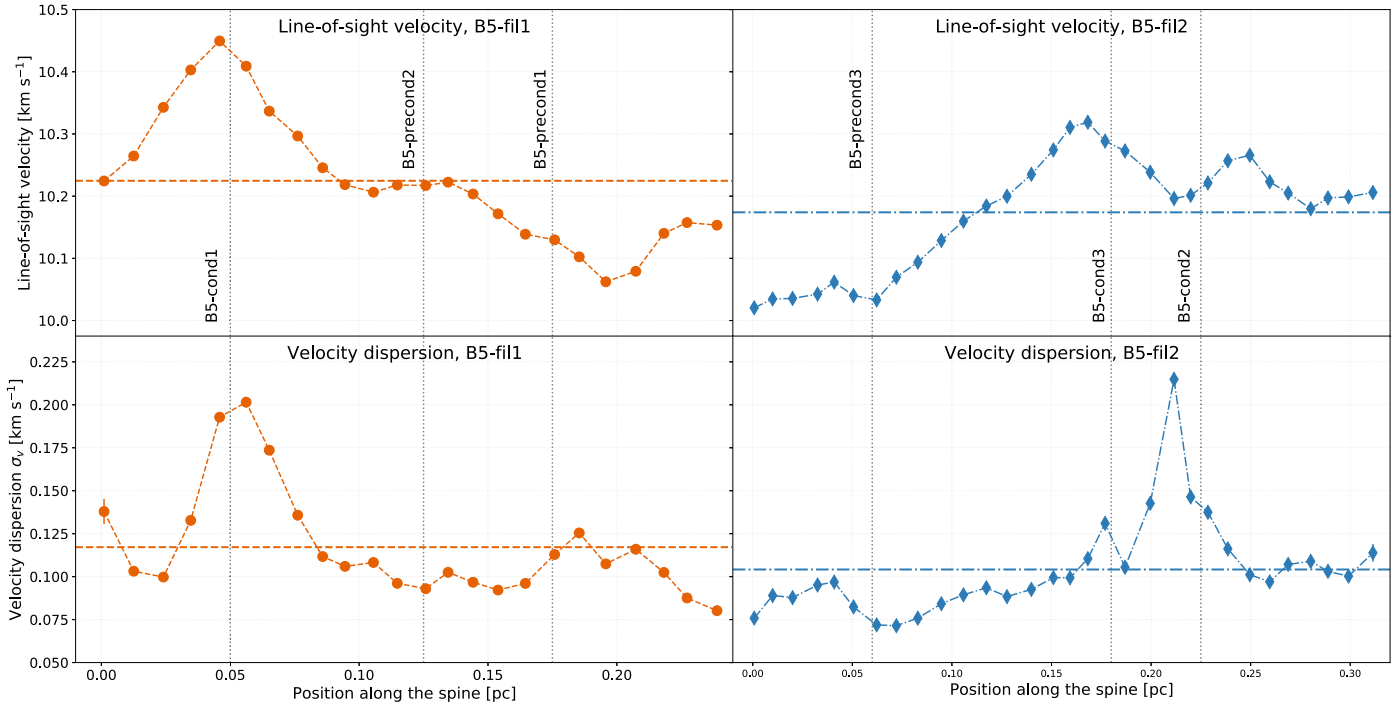

Figure 6. Kinematic properties along the spines of the filaments. Left: B5-fil1, marked with orange circles and a dashed line. Right: B5-fil2, marked with blue diamonds and a dashed–dotted line. Top: line-of-sight velocity $v_{\rm lsr}$. Bottom: velocity dispersion $\sigma_{\rm v}$. The uncertainties for the majority of the data points are located within the markers. The dashed and dashed–dotted horizontal lines mark the average values of the spine properties. The vertical gray dotted lines mark the location of the three condensations, as well as the precondensations. The position 0.0 starts to the south of the spine.

like, e.g., IC 5146 (Arzoumanian et al. 2011) using dust continuum emission maps. Monsch et al. (2018), on the other hand, reported the detection of a narrow filament, $R_{\rm flat} = 0.013$ pc (i.e., 2680 au), with a steep exponent, $p = 5.1$, in the Orion A OMC1 region using the dense gas tracer NH_3. Along the spine, we notice a trend of decreasing $R_{\rm flat}$ toward the condensations, i.e., toward increasing n_0. Similarly, we notice an increase in the exponent when $R_{\rm flat}$ increases. These (anti)correlations are further discussed in Section 4.5.

3.2.6. Kinematics

In Figure 6, we show the line-of-sight velocity $v_{\rm lsr}$ and the velocity dispersion $\sigma_{\rm v}$ along both filament spines. There is a mild gradient in correspondence with the condensations, suggestive of inflowing material. This has also been suggested by Hacar & Tafalla (2011), where they showed the velocity oscillations along filamentary structures in Taurus. It is noticeable that B5-cond1 falls at a peak, while B5-cond2 and B5-cond3 do not. This could be related to the protostar B5-IRS1 affecting the line-of-sight velocity structure in B5-fil2. The velocity dispersion $\sigma_{\rm v}$, including both thermal and nonthermal motions, shows an increase in B5-fil1 toward B5-cond1 and in B5-fil2 toward the location in between the other two condensations. This might be caused by the protostellar object B5-IRS1, which is located nearby.

4. Discussion

4.1. Similarities between Spine Profiles

We noticed that the spine profiles of B5-fil1 and B5-fil2 appear visually similar if one starts following them from the end at which their embedded condensations are located and scales them to the same length. To quantify this further, we have inverted the spine profiles of B5-fil2 shown in Figure 5; i.e., we follow the spine of this filament from north to south. We rescale the filament length by a factor of 0.767 to match it to the length of B5-fil1. We then interpolate the spine profiles of B5-fil2 and extract profile values at the same equidistant positions as for B5-fil1. An example of the resulting spine profiles of this procedure is shown for the peak intensity spine profile in the left panel of Figure 7. We then calculate the Pearson's R statistic between both filaments for each of the following properties: peak intensity, mass per unit length M/L, central density n_0, Plummer exponent p, $R_{\rm flat}$, and $\rm FWHM_d$. We apply a shift to the spine profiles of B5-fil2 and calculate the Pearson's R statistic to find the best alignment between the filaments. The variation of the Pearson's R values as a function of shift is shown in the right panel of Figure 7. The variation of the correlation is similar for all parameters. Shifting the spine profiles of B5-fil2 by 0.01 pc to the north of this filament results in a high correlation between all parameters. This shift aligns the position of B5-cond1 with that of B5-cond2.

4.2. Comparison with Herschel Filaments

The filaments we study here are embedded within the coherent core of B5. In this subsection, we compare the properties derived for these filaments to the properties of the Herschel filaments.

The Herschel Gould Belt Survey (HGBS; André et al. 2010) has mapped star-forming regions at five different wavelengths (70–500 μm), from which the HGBS team has derived H_2 column density maps at a native resolution of $\sim$36″ and a medium resolution of 18.″2 following the procedure presented in Palmeirim et al. (2013). In their recently published study, Arzoumanian et al. (2019) investigated eight of these star-forming regions and

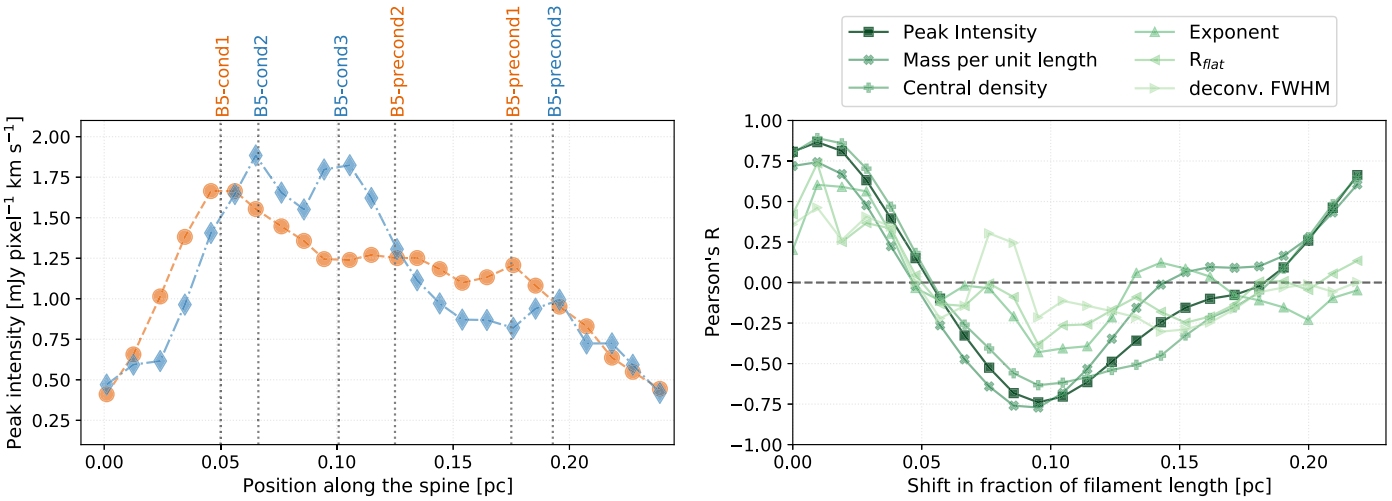

Figure 7. Left: same as Figure 5(a), but the spine profile of B5-fil2 is inverted and scaled. Right: correlation of different spine profiles between B5-fil1 and B5-fil2 as a function of relative shift along the spine. See Section 4.1 for details.

identified a total of ~600 individual filaments that have an aspect ratio >3. For this sample of filaments, they derived distributions of filament properties (see their Table 3), such as the length of the filaments $L = 0.66 \pm 0.46$ pc, the mass per unit length $M/L = 14 \pm 18\, M_\odot\, \mathrm{pc}^{-1}$, the central column density $N^0_{H_2} = (7.0 \pm 6.2) \times 10^{21}\, H_2\, \mathrm{cm}^{-2}$, the Plummer profile exponent $p = 2.2 \pm 0.3$, and the deconvolved filament width $\mathrm{FWHM_d} = 0.1 \pm 0.05$ pc.

We compare this to the results from fitting the average profiles of the B5 filaments (see Table 2). The B5 filaments are shorter ($L = 0.28$ pc), more supercritical ($M/L = 41.2\, M_\odot\, \mathrm{pc}^{-1}$), steeper ($p = 3.0$), and narrower ($\mathrm{FWHM_d} = 0.03$ pc) than the Herschel filaments.

When using molecular lines to study filaments, properties such as the inferred filament widths seem to be dependent on the observed molecule. For 55 dense fibers identified in Orion's Integral Shape Filament, Hacar et al. (2018) found the distribution of filament width peaking at 0.035 pc using N_2H^+. Panopoulou et al. (2014), on the other hand, inferred a broad distribution of filament width peaking at 0.4 pc in the Taurus molecular cloud using ^{13}CO. Studying the Orion A molecular cloud using C^{18}O, Suri et al. (2019) found a varying filament width between 0.02 and 0.3 pc, mostly in agreement with the dust continuum–based study by Arzoumanian et al. (2019). They attributed the large spread to the amount of substructure present within a filament. In many of these cases, however, the spatial resolution of the molecular line data used to determine the filament widths is often better by a factor of 2–4 compared to the medium-resolution H_2 column density map derived from the Herschel continuum observations.

The difference in the filament properties found for the B5 filaments could be due to different angular resolution or the fact that ammonia is a high-density tracer and, as such, picks out only the spine of the filaments.

Angular resolution. We smooth the high-resolution NH_3(1,1) integrated intensity map to the medium resolution of the Herschel column density map, i.e., 18.″2. We use the filament spine determined using fil_finder on the high-resolution NH_3(1,1) integrated intensity map and extract equidistant cuts perpendicular to the spines. We average the cuts and apply the same fitting procedure as described in Section 3.2.1. The details of this processing, as well as the results, are given in Appendix C. The average profiles of the B5 filaments become even steeper ($p = 4.14$), and while their width increases, they remain narrow ($\mathrm{FWHM_d} = 0.05$ pc).

High-density tracer versus continuum. We use the medium-resolution H_2 column density map derived for Perseus that is publicly available on the HGBS website.[10] We apply the same processing as for the smoothed NH_3(1,1) integrated intensity map described above. The details of this processing are given in Appendix C. The averaged profiles of the B5 filaments remain steep ($p = 3.33$), and their widths increase marginally ($\mathrm{FWHM_d} = 0.06$ pc). The central column density is higher ($N^0_{H_2} = 1.3 \times 10^{22}\, H_2\, \mathrm{cm}^{-2}$) compared to the Herschel filaments. There is only a very small difference between the fitting results of the smoothed high-density tracer and the H_2 column density map, indicating that NH_3(1,1) is not filtering out the extended wings of filaments and hence is a good tracer of filamentary structures.

In summary, the physical properties (length, width, volume density, density profile) of the filamentary substructure present within the coherent core of B5 are significantly different from those measured in Herschel filaments. This is not surprising, considering the higher-density environment within which the B5 filamentary substructure has formed, and it suggests that environmental conditions play a crucial role in shaping the physical characteristics of filaments in general.

4.3. Can the Filaments Be Magnetically Supported?

Both filaments are supercritical, but the turbulence present in the coherent core (sonic Mach number, $M_s = \sigma_{nt}/c_s = 0.5$) is insufficient to support them against gravitational collapse. Hence, they should be in a state of collapse—unless magnetic fields are present, which could provide additional support against gravitational collapse (Fiege & Pudritz 2000a; Seifried & Walch 2015). This poses the question of how strong a magnetic field would need to be to stabilize the filaments.

We present here a first attempt to estimate the magnetic field strength in B5, which has not yet been measured. A toroidal field does not stabilize the filament against radial collapse (Fiege & Pudritz 2000a). A poloidal field that is perpendicular to the spine of the filament has also been found to not stabilize it (Seifried & Walch 2015). This leaves a poloidal field that is

[10] http://www.herschel.fr/cea/gouldbelt/en

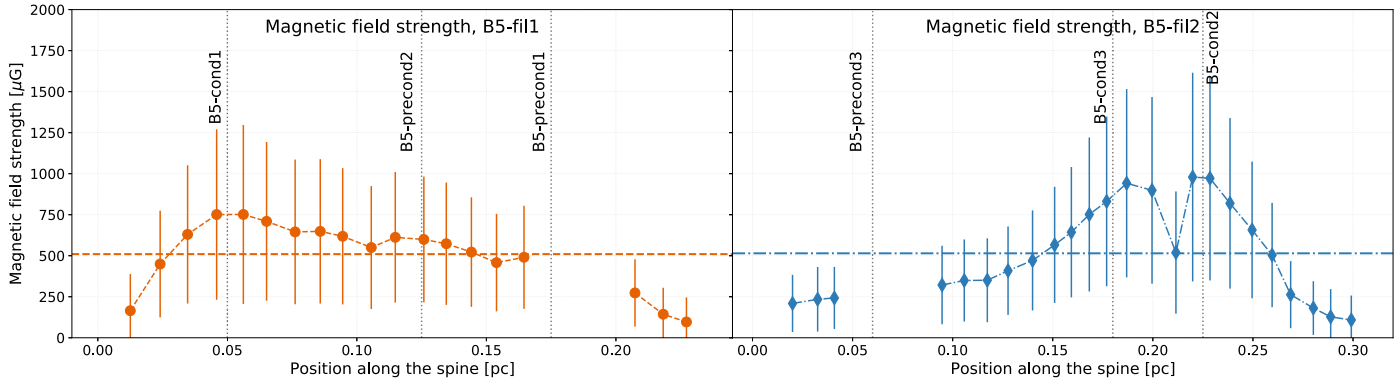

Figure 8. Local variation of the estimated magnetic field strength B_z required to stabilize the filament for B5-fil1 (left) and B5-fil2 (right). The dashed and dashed–dotted horizontal lines mark the average values of the magnetic field strength. The vertical gray dotted lines mark the location of the condensations, as well as the precondensations. The position 0.0 starts to the south of the spine. The holes are due to the kinetic temperature being undetermined at the respective positions.

parallel to the filament, which has indeed been found to stabilize a filament (Fiege & Pudritz 2000a; Seifried & Walch 2015). We use this orientation to estimate the minimum magnetic field required to fully stabilize the filaments against collapse, which would ultimately prevent any fragmentation from happening.

The critical mass per unit length for an isothermal cylinder is given in Equation (5) (Ostriker 1964). The cylinder can be further stabilized by turbulence and magnetic field. Taking the turbulence into account, Fiege & Pudritz (2000a) derived a modified critical mass per unit length (see their Equation (12)),

$$(M/L)_{\rm crit,nt} = \frac{2\sigma_{\rm v}^2}{G}, \tag{8}$$

where $\sigma_{\rm v}$ is the velocity dispersion of the gas including thermal and nonthermal (nt) motions (see Equation (1)).

Taking the magnetic field B_z parallel to the spine of the filament into account, Fiege & Pudritz (2000a) determined

$$(M/L)_{\rm crit,mag} = \frac{2\sigma_{\rm v}^2 + \frac{B_z^2}{4\pi\mu_{\rm p} m_{\rm H} n_0}}{G}, \tag{9}$$

where $\mu_{\rm p} = 2.37$ is the mean molecular weight per free particle (Kauffmann et al. 2008), and $m_{\rm H}$ is the hydrogen atom mass. Assuming that our filaments are gravitationally stable, i.e., the observationally measured mass per unit length $(M/L)_{\rm obs}$ equals $(M/L)_{\rm crit,mag}$, evaluating Equation (9) for the magnetic field B_z, and using Equation (8) yields

$$B_z = \sigma_v \sqrt{8\pi\mu_p m_{\rm H} n_0 \left(\frac{(M/L)_{\rm obs}}{(M/L)_{\rm crit,nt}} - 1 \right)}. \tag{10}$$

In Figure 8, we show the distribution of the required magnetic field strength B_z to support the filaments. The mean B_z is 510 μG for B5-fil1 and 515 μG for B5-fil2. We notice an increase in the required magnetic field strength toward the condensations up to values of $\sim$950 μG. Since fragmentation seems to be already ongoing toward the condensations, this is not unexpected. We exclude the tips of the filaments, as they deviate from the cylinder assumption. We note that the holes in the profiles originate from the kinetic temperature being undetermined at the respective position.

Another region, also embedded in the Perseus molecular cloud and hence sharing the same parental molecular cloud as B5, is Barnard 1 (B1). The B1 clump hosts several pre- and protostellar cores at different evolutionary stages. Recently, Coudé et al. (2019) determined the magnetic field strength of B1 to be 120 μG using JCMT polarization data. Chapman et al. (2011) reported that the plane-of-the-sky magnetic field strength in the nearby star-forming region Taurus ranged from 10 to 40 μG using near-infrared polarization observations. Sugitani et al. (2011), on the other hand, determined a rough estimate of the magnetic field strength in the Serpens cloud to be a few $\times$ 100 μG. Liu et al. (2019) reported magnetic field strengths toward a low-mass starless core in the ρ Ophiuchus cloud of 103–213 μG using three different methods and JCMT 850 μm dust polarization observations. Also toward Ophiuchius, Pattle et al. (2021) reported magnetic field strengths ranging between 72 and 366 μG.

Our inferred value of the magnetic field strength is an upper limit. It exceeds many of the measured values in other (low-mass) star-forming regions or clumps. So, while it may still be possible that the filaments could be marginally supported by magnetic pressure, additional observations are required to quantify this.

4.4. Fragmentation

The simplest case of cylindrical fragmentation is that of an isothermal, pressure-supported, infinitely long filament. The gravitational fragmentation of such a system has a critical wavelength of $\lambda_{\rm crit} = 3.94\,H$, where

$$H^2 = \frac{2\,c_s^2}{\pi\,G\,\mu\,n_0} \tag{11}$$

(Stodólkiewicz 1963; Ostriker 1964; Hacar & Tafalla 2011). Taking the average central density of the filaments of $n_0 = 10^6\,{\rm cm}^{-3}$ and a gas temperature of 9 K yields a critical wavelength of $\lambda_{\rm crit} = 7400$ au (0.04 pc). We determine the closest separation between two structures along the filament spines to be 0.045 pc, between B5-cond2 and B5-cond3. The separation between B5-cond1 and B5-precond2 along the filament spine is 0.05 pc.

But this approach neglects the influence of turbulence and magnetic fields on the critical wavelength. Fiege & Pudritz (2000b) investigated the effect of the magnetic field and its orientation on the critical wavelength. For a poloidal magnetic field parallel to the filament spine, they found that the scale for the separation of the fragments increases with increasing magnetic field strength. This could mean that some of our

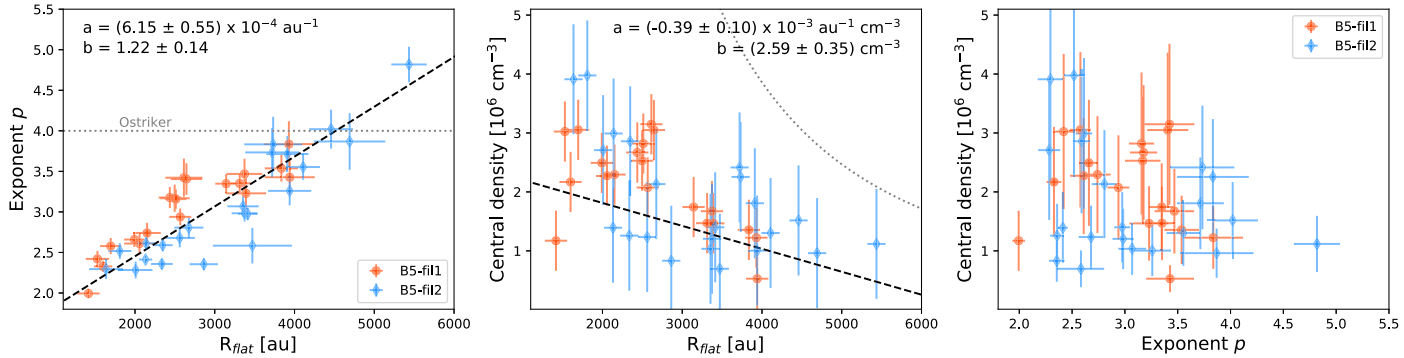

Figure 9. Left: correlation between exponent p and flattening radius $R_{\rm flat}$. Middle: anticorrelation between central density n_0 and flattening radius $R_{\rm flat}$. The dotted line marks the critical length $\lambda_{\rm crit} = 3.94H$, with H as given in Equation (11) (Ostriker 1964). Right: relation between central density n_0 and exponent p.

identified substructure within the filaments is spaced too closely. However, to further investigate the influence of the magnetic field on the separation of the fragments will require a measurement of the magnetic field orientation and strength.

4.5. Filament Evolution

As mentioned in Section 3.2.5, we notice a relation between $R_{\rm flat}$, n_0, and the exponent p along the spines of these filaments. To investigate this further, we plot the relation of all three parameters with each other in Figure 9. Especially clear is the correlation between the exponent p and $R_{\rm flat}$. The anticorrelation between the central density and $R_{\rm flat}$ is less clear due to the high error associated with the central density, to which the uncertainty in the temperature determination contributes the most. The best-fit linear fits shown in Figure 9 take the associated uncertainties into account. The emerging trend is that dense filaments are narrower, and filaments deviate from the fiducial isothermal filament model as they become denser and narrower.

To derive an empirical relation between all three parameters, we fit a plane to the three-dimensional parameter space,

$$R_{\rm flat} = \alpha_1 \frac{n_0}{10^6\ {\rm cm}^{-3}} + \alpha_2\, p + \beta, \tag{12}$$

where α_1 and α_2 are scaling parameters and β is the intercept of the plane. Since all three parameters have a measurement error associated with them, we use the Hyper-fit package (Robotham & Obreschkow 2015) to fit a plane in 3D. This package allows us to fit linear models to multidimensional data with multivariate Gaussian uncertainties and provides access to a multitude of fitting algorithms. We employ the Nelder–Mead algorithm and obtain the following values: $\alpha_1 = -320 \pm 71$, $\alpha_2 = 1544 \pm 111$, and $\beta = -1153 \pm 360$. Figure 10 shows the reprojected hyperplane.

This provides the first observational prescription of the evolution of the physical parameters of the filaments dependent on $R_{\rm flat}$. Although this relation might not be universal, it shows the first clear evolution of a filament that is collapsing or fragmenting, revealing the global trends.

For an isothermal filament in hydrostatic equilibrium (exponent $p = 4$), Arzoumanian et al. (2011) stated that the flattening radius $R_{\rm flat}$ corresponds to the thermal Jeans length $\lambda_{\rm J}$, which is anticorrelated with the central column density Σ_0. They investigated three low-mass star-forming filaments, Aquila, IC 5146, and Polaris, and found a lack of anticorrelation between the filament widths, which they determine as the deconvolved FWHM from the Gaussian fit to the profile, and the column density (see their Figure 7). However, from fitting a Plummer-like function to the mean column density profile of the filaments, they determined that the exponent p ranged between 1.5 and 2.5, i.e., less steep than the exponents of B5-fil1 and B5-fil2. They determined a flattening radius $R_{\rm flat} = 2000$–$16{,}000$ au; i.e., only a small subsection has similar values as B5-fil1 and B5-fil2. Similarly, Suri et al. (2019) analyzed $C^{18}O$ observations of the high-mass star-forming region Orion A. They determined the widths of the 625 individual, relatively short (<1.7 pc) filaments that they identified. Using the column density map derived from Herschel data (Stutz & Kainulainen 2015), they found no (anti)correlation between filament widths and column density (see their Figure 11). On the other hand, they did find a correlation between filament widths and number of shoulders in the radial intensity profiles detected, suggestive of (unresolved) substructures within the filaments. Therefore, it is possible that their analysis is, e.g., affected by optical depth effects, or the peak column density could be underestimated due to the large Herschel beam.

It could be possible that ammonia is tracing higher-density material and hence we are able to see the expected inverse relation between $R_{\rm flat}$ and the central density n_0. A similar investigation for other filaments would be needed to confirm the relationship observationally. In addition, numerical simulations are required to investigate if and under which circumstances these correlations appear.

5. Summary

In this paper, we analyze previously published combined VLA and GBT ammonia data together with JCMT continuum data of B5. Embedded in the coherent region, we find two clumps, one quiescent and the other containing two filamentary structures. Embedded in the filaments are three condensations, and along the spines of the filaments, we find signs of additional clumpy structures. We characterize the filament properties in detail by fitting both a Plummer function and a Gaussian to equidistant cuts extracted perpendicular to the filament spines.

1. Both filaments are narrow and dense. Their deconvolved FWHMs range between 6200 and 7000 au, i.e., $2\times$ the flattening radius of the Plummer function, and their average central density is on the order of 10^6 cm^{-3}. Their aspect ratios are 17:1 and 10:1.

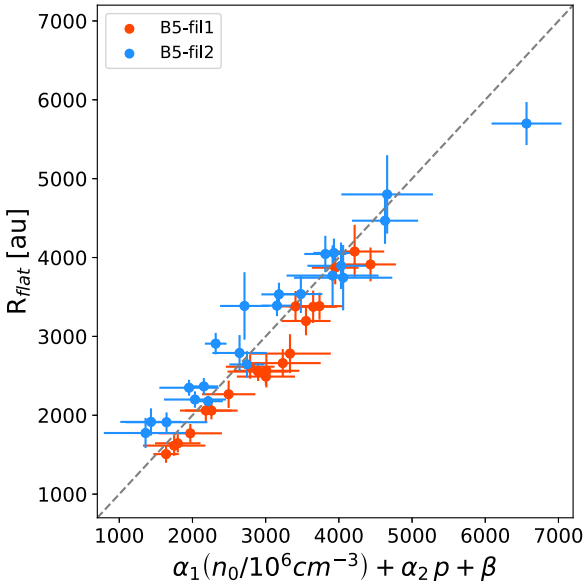

Figure 10. Correlation between the flattening radius $R_{\rm flat}$, central density n_0, and exponent p along the filament spines.

2. The line-of-sight velocity is $\sim$10.2 km s^{-1}, and the velocity dispersion along the filament spines is 0.1 km s^{-1} but increases toward the location of the condensations.
3. Both filaments are supercritical, exhibiting mass per unit length values of $\sim 80\,M_\odot$ pc^{-1}. Locally, this value increases up to $150\,M_\odot$ pc^{-1}.
4. We estimate the required magnetic field strength to stabilize the filaments, ultimately stopping further fragmentation, to be on the order of $\sim$500 μG. Since we see signs of ongoing fragmentation, we conclude that this magnetic field strength is an upper limit.
5. We fit the radial profiles perpendicular to the filament spines and see a variation in power-law exponent and width along the filament. Their maxima are coincident with the peak positions of the condensations, which could be related to the filament evolution.
6. We find a strong correlation between the Plummer exponent and the flattening radius. We also find an anticorrelation between the central density and this flattening radius, suggestive of contraction. The measurements of these three parameters (central density, Plummer exponent, and flattening radius) fall in a plane, and we derive their empirical relation. Numerical simulations are needed to see if and under what circumstances these correlations are being seen.

We thank the anonymous referee for helpful comments that improved the paper. A.S., J.E.P., P.C., M.J.M., and D.S.C. acknowledge the support of the Max Planck Society. G.A.F. acknowledges financial support from the State Agency for Research of the Spanish MCIU through the AYA2017-84390-C2-1-R grant (cofunded by FEDER) and the "Center of Excellence Severo Ochoa" award for the Instituto de Astrofísica de Andalucia (SEV-2017-0709). The National Radio Astronomy Observatory and the Green Bank Observatory are facilities of the National Science Foundation operated under cooperative agreement by Associated Universities, Inc. This research has made use of data from the Herschel Gould Belt Survey (HGBS) project (http://gouldbelt-herschel.cea.fr). The HGBS is a Herschel Key Programme jointly carried out by SPIRE Specialist Astronomy Group 3 (SAG 3), scientists of several institutes in the PACS Consortium (CEA Saclay, INAF-IFSI Rome and INAF-Arcetri, KU Leuven, MPIA Heidelberg), and scientists of the Herschel Science Center (HSC).

Facilities: VLA, GBT, JCMT.

Software: aplpy (v.2.0.3; Robitaille & Bressert 2012), astrodendro (v0.2.0; Rosolowsky et al. 2008), astropy (v4.0.2; Astropy Collaboration et al. 2013, 2018), fil-finder (v1.7; Koch & Rosolowsky 2015), hyper-fit (Robotham & Obreschkow 2015), lmfit (v1.0.1; Newville et al. 2016), numpy (v.1.19.2; Van Der Walt et al. 2011), pyspeckit (v0.1.23; Ginsburg & Mirocha 2011), radfil (v1.1.2; Zucker & Chen 2018), spectral-cube (v0.5.0; Robitaille et al. 2016).

Appendix A
Line Fitting

We simultaneously fit the NH_3(1,1) and (2,2) lines using the `cold-ammonia` model (Friesen et al. 2017) in `pySpecKit` (Ginsburg & Mirocha 2011). This model assumes that both transitions have the same excitation temperature $T_{\rm ex}$ and that only the (1,1) and (2,2) levels are populated; i.e., the model does not present hyperfine anomalies (Stutzki et al. 1984). The best fit is obtained by minimizing the χ^2, which also provides an uncertainty for each parameter. Input parameter guesses are based on (a) the velocity centroid of the line for $v_{\rm lsr}$, (b) the intensity-weighted second moment of the velocity around the centroid for the velocity dispersion σ_v, (c) $\log_{10}(N/{\rm cm}^{-2}) = 14.5$, (d) $T_K = 12$ K, and (e) $T_{\rm ex} = 3$ K, based on the temperature of the cosmic-ray background radiation (2.73 K). We include all pixels in the fit where the NH_3(1,1) line has an S/N $\geqslant 5$. We account for the channel response by applying the following correction to the velocity dispersion:

$$\sigma = \sqrt{\sigma^2_{\rm v,fit} - \frac{dv_{\rm chan}}{2\sqrt{2\ln 2}}}, \tag{A1}$$

where $\sigma_{\rm v,fit}$ is the velocity dispersion from the fit and $dv_{\rm chan}$ is the channel width.

We perform additional masking to remove poor fit results on a pixel-by-pixel basis for each parameter map. The line-of-sight velocity and velocity dispersion can be reliably obtained with a good fit of the NH_3(1,1) line; therefore, we flag only those pixels with an associated uncertainty of $>$0.02 km s^{-1} in $v_{\rm lsr}$ or σ_v. Determination of the excitation and kinetic temperatures, $T_{\rm ex}$ and T_K, as well as the ammonia column density, $N_{\rm NH_3}$, requires a good fit for both the NH_3(1,1) and NH_3(2,2) transitions. An inaccurate kinetic temperature yields an erroneous excitation temperature. Hence, we require an S/N $\geqslant 12$ for the NH_3(1,1) line and an S/N $\geqslant 3$ for the NH_3(2,2) line, as well as the associated uncertainties of the temperature fits $\sigma_{\rm fit,T} < 2$ K. For the uncertainty of the ammonia column density, we require $\sigma_{\rm fit,log_{10}(N/cm^{-2})} < 1.0$. In addition to that, an accurate determination of the ammonia column density depends on a good determination of both temperatures, $T_{\rm ex}$ and

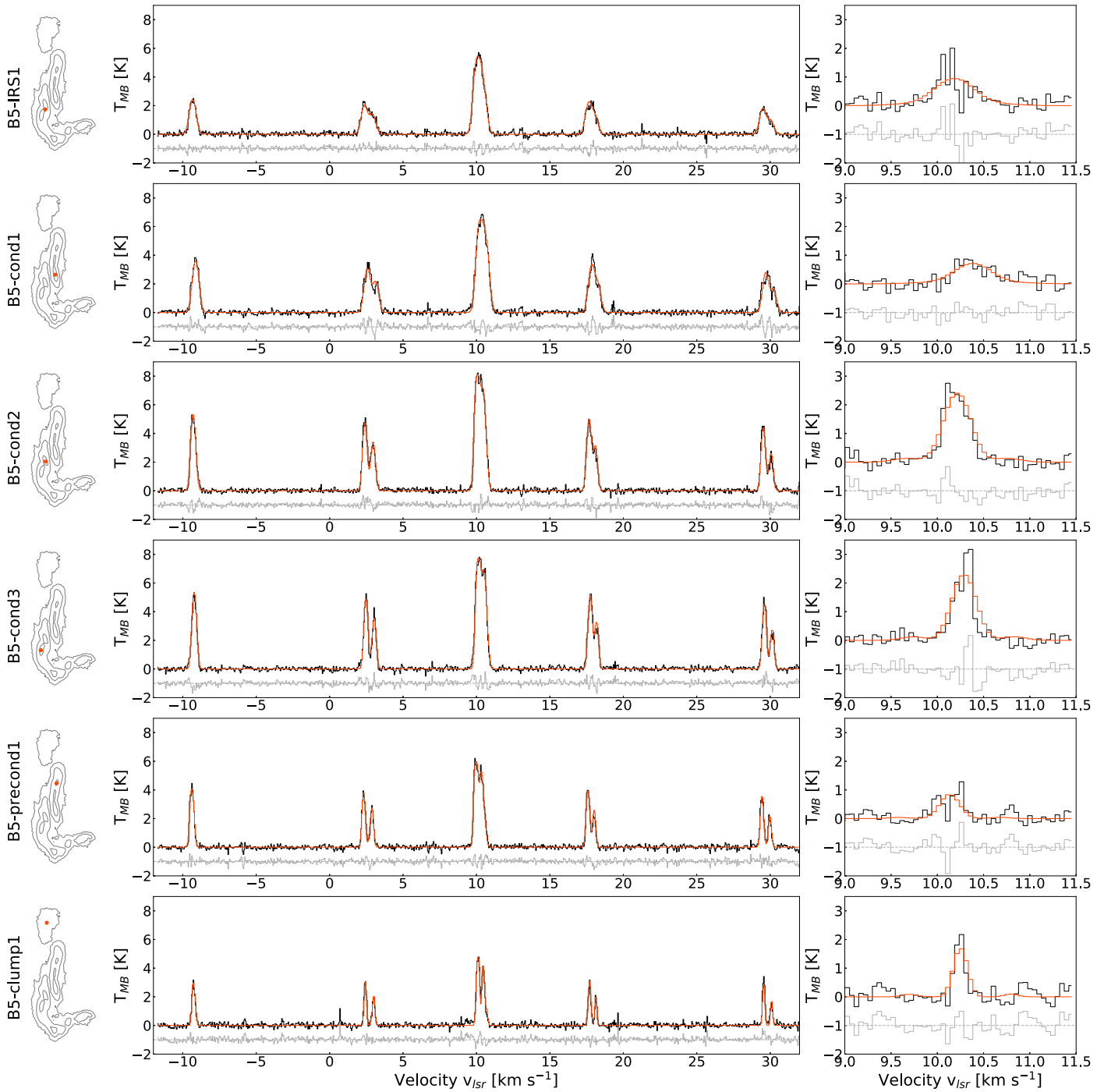

Figure 11. Top to bottom: sample spectra of ammonia toward six different positions in B5. Left column: contour map of B5, where the orange dot marks the location toward which the spectra have been extracted. Middle column: beam-averaged spectrum of NH_3(1,1). The observed spectrum is plotted in black, and the best-fit model is shown in orange. The hyperfine splitting is clearly visible in each spectrum. Right column: beam-averaged spectrum of NH_3(2,2).

T_K (Ho & Townes 1983; Friesen et al. 2009). Hence, if a pixel has been flagged in the temperature maps, it will also be flagged in the column density map.

Figure 11 shows the NH_3(1,1) and NH_3(2,2) beam-averaged spectra of six regions in the map corresponding to the YSO B5-IRS1, the three condensations, B5-precond1, and B5-clump1. Their respective locations are indicated by the orange dots in the contour maps. The spectra clearly show the hyperfine splitting in the NH_3(1,1) transition thanks to the narrow velocity dispersions. The final maps of ammonia column density N_{NH_3}, kinetic temperature T_K, center velocity v_{lsr}, and velocity dispersion σ_v are shown in Figure 2.

Appendix B
Conversion Factors

B.1. Ammonia-to-mass Conversion by Scaling

We measure the flux density in B5-cond1 in the JCMT 450 μm map, which is bright and without a protostar, to estimate its mass. To determine the total mass of the filaments,

we use the JCMT 450 μm map to scale the NH_3(1,1) integrated emission map, which is more sensitive to the filamentary structure. In the first step, we calculate the flux-to-mass conversion factor ξ based on the conditions in B5-cond1 using

$$\xi = \mathcal{G}\frac{d^2}{\kappa_\nu B_\nu(T_d)}, \tag{B1}$$

where $\mathcal{G}$ is the gas-to-dust ratio ($\mathcal{G} = 100$; Hildebrand 1983), d is the distance to the object ($d = (302 \pm 21)$ pc; Zucker et al. 2018), κ_ν is the dust absorption coefficient at the frequency ν, and $B_\nu(T_d)$ is the Planck function evaluated at the dust temperature T_d.

To determine the dust temperature, we fit a Gaussian to the distribution of kinetic temperatures within the filaments (see Appendix A) and obtain a mean temperature of $T_k = (9 \pm 1)$ K. This assumes that the dust temperature is coupled to the gas temperature. We also assume that the dust is optically thin, covered in thin to thick ice mantles, and coagulated at $(10^5$–$10^7)$ cm^{-3}. We interpolate the corresponding tabulated dust opacities provided by Ossenkopf & Henning (1994) to a wavelength of 450 μm and then determine a mean dust absorption coefficient $\kappa_{450} = (6.4 \pm 0.8)$ cm^2 g^{-1}. With that, we derive a SCUBA flux-to-mass conversion factor of $\xi = (0.5 \pm 0.2)\, M_\odot\, \mathrm{Jy}^{-1}$.

We determine the background emission for both the JCMT 450 μm map and the integrated NH_3(1,1) map as the lowest-value pixel within the contour of B5-cond1. We note that this will yield very conservative mass estimates. For B5-cond1, we measure a background-corrected flux density of 0.99 Jy in the JCMT 450 μm map. For the same condensation, we measure a background-corrected flux density of 0.35 Jy in the integrated NH_3(1,1) map. This yields an ammonia-to-mass conversion factor of $(1.5 \pm 0.7)\, M_\odot\, \mathrm{Jy}^{-1}$.

B.2. Ammonia-to-mass Conversion from Column Density

We calculate the mass from the ammonia column density map on a pixel-by-pixel basis using

$$M = \mu_{H_2}\, m_H\, A_{\mathrm{pixel}}\, \frac{N_{NH_3}}{X_{NH_3}}, \tag{B2}$$

where μ_{H_2} is the molecular weight per hydrogen molecule ($\mu_{H_2} = 2.8$; Kauffmann et al. 2008), m_H is the atomic hydrogen mass, A_{pixel} is the size of the pixel (assuming a distance of $d = 302$ pc), N_{NH_3} is the ammonia column density from the fit (see Appendix A), and X_{NH_3} is the abundance of ammonia with respect to H_2. For a sample of clouds with similar conditions, Friesen et al. (2017) determined the abundance of ammonia with respect to H_2 to be $X_{NH_3} = 10^{-8.5}$, on average.

B.3. Comparison

The resulting mass maps for the filaments are shown in Figure 12. They agree within a factor of 2 with each other. The mass map derived from the column density is a factor of 2 higher compared to the mass map derived by scaling the continuum. The residual between both maps is smooth and does not show any strong gradients. All mass-dependent calculations in this work were performed on the basis of the mass map derived with the dust-scaling method.

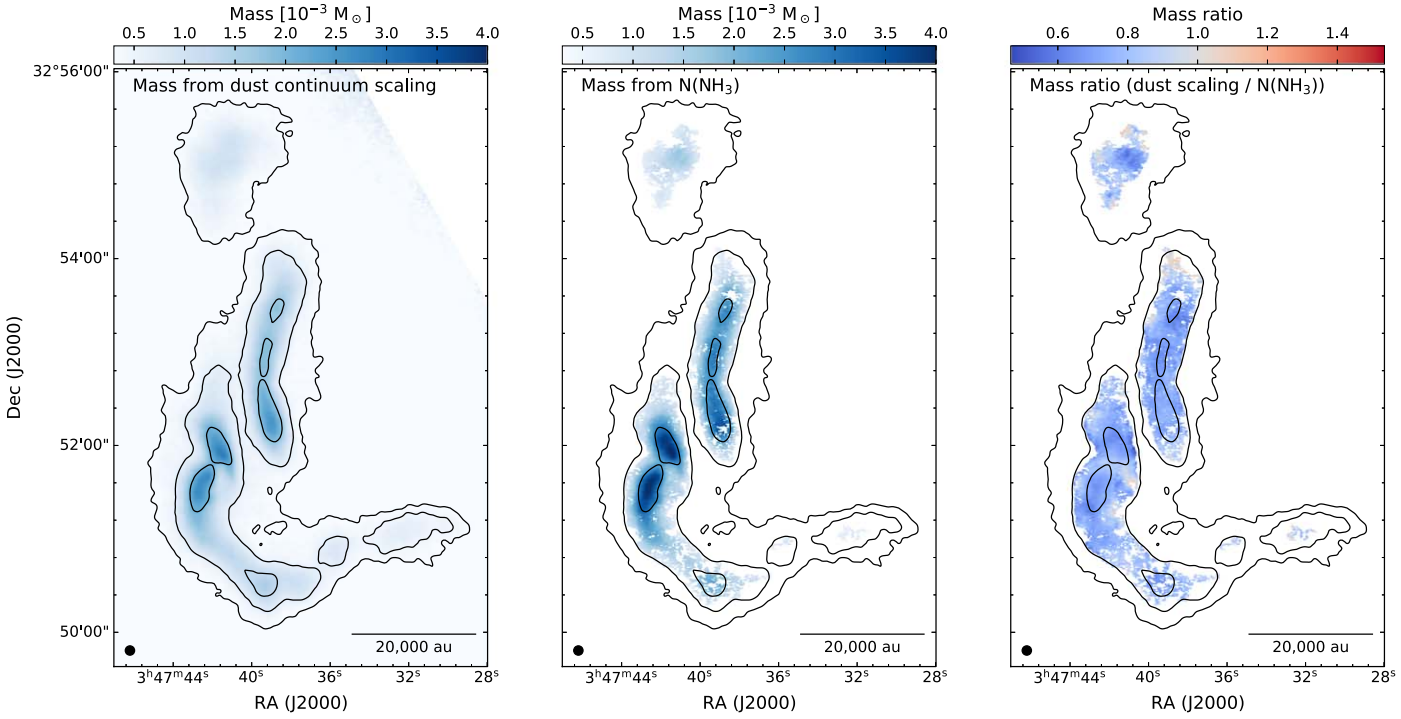

Figure 12. Left: mass map derived from scaling the VLA+GBT NH_3 integrated intensity map based on the mass scaling factor derived from the JCMT 450 μm dust continuum map. Middle: mass map derived from the NH_3 column density maps obtained from the line fitting (see Appendix A). Right: ratio map of the left and middle panels. The scale bar is shown in the bottom right corner of each panel.

Appendix C
Comparison of Filament Width at 18.″2 Resolution

As part of the HGBS (André et al. 2010), B5 was observed with Herschel PACS and SPIRE. The H_2 column density maps at two different spatial resolutions (36″ and 18.″2) are available on the HGBS website. The original resolution H_2 column density map was derived from spectral energy distribution fitting of the 160–500 μm maps on a pixel-to-pixel basis (for details, see, e.g., Pezzuto et al. 2012, 2021; Könyves et al. 2015). The 18.″2 resolution H_2 column density map was determined using a multiscale decomposition technique as described in Palmeirim et al. (2013).

We convolve our VLA+GBT NH_3(1,1) integrated intensity map to the same resolution as the medium-resolution H_2 column density map. Both maps are shown in the top row of Figure 13. We use the same method as described in Section 3.2.1 to extract equidistant cuts along the filament spines. We calculate the mean of the cuts and first fit a constant to determine the background emission level followed by fitting a Gaussian profile to the innermost part. For the profiles of the H_2 column density map, we adjust the range for the background emission fitting, since the emission is more extended compared to the NH_3 integrated intensity map. The fitting ranges for the Gaussian and Plummer fits are adjusted slightly to exclude contamination from nearby structures. The fit ranges are indicated with vertical lines in panels (c) and (d) in Figure 13. The fit results are summarized in Table 3 and discussed in Section 4.2.

Table 3
Results of Fitting the Plummer and Gaussian Functions to the Average Profiles for Three Data Sets

Source	Fit Function	Data Set	Parameters				Evaluation
B5-fil1	Plummer[a]		p	$R_{\rm flat}$ [au]	A[b]	bkg[b,c]	AIC
		NH_3, 6″	2.0[d]	1220 ± 40	1.184 ± 0.019	0.060 ± 0.001	−1150
		NH_3, 18.″2	2.0[d]	2080 ± 60	0.826 ± 0.013	0.073 ± 0.001	−1132
		Herschel, 18.″2	2.0[d]	3890 ± 50	1.858 ± 0.008	0.293 ± 0.002	−828
		NH_3, 6″	2.91 ± 0.06	2590 ± 80	1.090 ± 0.007	0.060 ± 0.001	−1462
		NH_3, 18.″2	3.74 ± 0.06	5420 ± 100	0.767 ± 0.002	0.073 ± 0.001	−1741
		Herschel, 18.″2	3.01 ± 0.11	6660 ± 260	1.818 ± 0.005	0.293 ± 0.002	−980
		NH_3, 6″	4.0[d]	3790 ± 40	1.052 ± 0.008	0.060 ± 0.001	−1349
		NH_3, 18.″2	4.0[d]	5800 ± 20	0.764 ± 0.002	0.073 ± 0.001	−1729
		Herschel, 18.″2	4.0[d]	8690 ± 50	1.802 ± 0.004	0.293 ± 0.002	−948
	Gaussian[a]		$A_{\rm G}$	$\sigma_{\rm G}$ [au]	$\mu_{\rm G}$ [au]	bkg[b,c]	AIC
		NH_3, 6″	6449 ± 23	2530 ± 10	−54 ± 9	0.060 ± 0.001	−640
		NH_3, 18.″2	6946 ± 16	3700 ± 10	40 ± 6	0.073 ± 0.001	−805
		Herschel, 18.″2	23,153 ± 74	5140 ± 20	−127 ± 8	0.293 ± 0.002	−718
B5-fil2	Plummer[a]		p	$R_{\rm flat}$ [au]	A[b]	bkg[b,c]	AIC
		NH_3, 6″	2.0[d]	1470 ± 40	1.134 ± 0.017	0.0494 ± 0.0004	−1161
		NH_3, 18.″2	2.0[d]	2300 ± 80	0.841 ± 0.014	0.0517 ± 0.0003	−1061
		Herschel, 18.″2	2.0[d]	2750 ± 70	1.443 ± 0.018	0.3964 ± 0.0009	−892
		NH_3, 6″	2.98 ± 0.05	3140 ± 80	1.049 ± 0.006	0.0494 ± 0.0004	−1537
		NH_3, 18.″2	4.85 ± 0.29	7020 ± 270	0.774 ± 0.005	0.0517 ± 0.0003	−1482
		Herschel, 18.″2	3.64 ± 0.10	6710 ± 200	1.359 ± 0.005	0.3964 ± 0.0009	−1295
		NH_3, 6″	4.0[d]	4440 ± 40	1.016 ± 0.006	0.0494 ± 0.0004	−1412
		NH_3, 18.″2	4.0[d]	6240 ± 50	0.785 ± 0.004	0.0517 ± 0.0003	−1473
		Herschel, 18.″2	4.0[d]	7370 ± 40	1.351 ± 0.005	0.3964 ± 0.0009	−1287
	Gaussian[a]		$A_{\rm G}$	$\sigma_{\rm G}$ [au]	$\mu_{\rm G}$ [au]	bkg[b,c]	AIC
		NH_3, 6″	7063 ± 29	2830 ± 20	−39 ± 10	0.0494 ± 0.0004	−627
		NH_3, 18.″2	7904 ± 20	4130 ± 10	136 ± 7	0.0517 ± 0.0003	−826
		Herschel, 18.″2	16,227 ± 94	4880 ± 30	201 ± 15	0.3964 ± 0.0009	−662

Notes.
[a] The fitting ranges where identical and kept fixed.
[b] Units for the NH_3 map are mJy km s^{-1}; units for the column density map derived from Herschel continuum maps are 10^{22} H_2 cm^{-2}.
[c] The background (bkg) has been determined by first fitting a constant and was fixed in the subsequent Plummer/Gaussian fit.
[d] The parameter has been fixed.

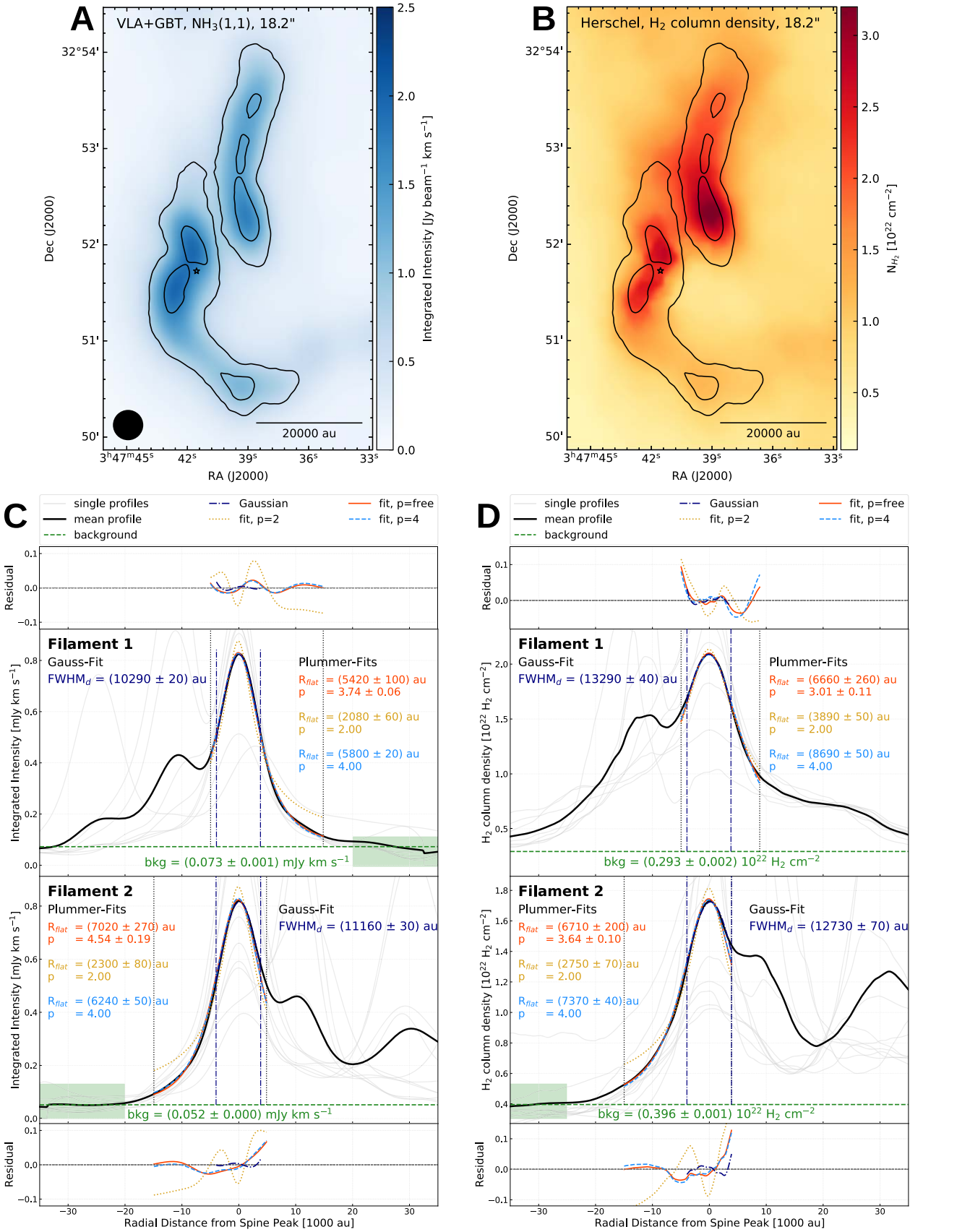

Figure 13. Panel (a): $NH_3(1,1)$ integrated intensity map convolved to a spatial resolution of 18.″2. Panel (b): H_2 column density map at a resolution of 18.″2 derived from Herschel observations (Palmeirim et al. 2013). Panel (c): same as Figure 4 but for a lower spatial resolution. Panel (d): same as Figure 4 but for the H_2 column density map at 18.″2 resolution.

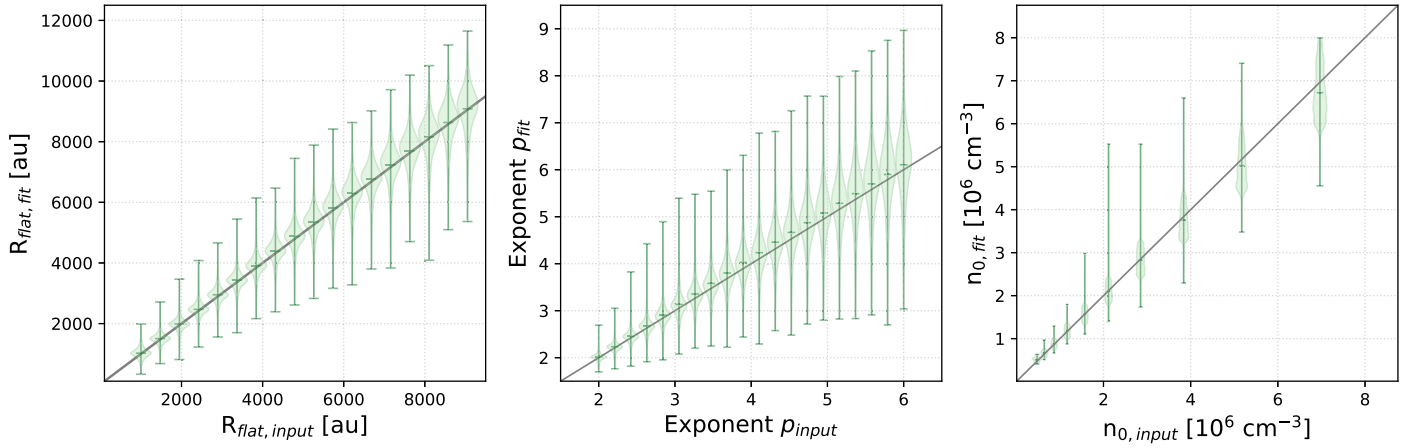

Figure 14. Relation between fitted and input parameters of synthetic Plummer profiles. Left: $R_{\rm flat}$. Middle: exponent p. Right: central density n_0. The solid gray line marks the 1:1 relation.

Appendix D
Assessing Degeneracy in Fitting High-contrast Plummer Profiles

We examine the reliability of the filament properties using our fitting method outlined in Section 3.2.1. To this end, we generate a suite of synthetic profiles with given $R_{\rm flat}$, exponent p, and peak intensity A to sample the parameter space uniformly. We set the constant background level to the mean of the background level of the fitted profiles in this work (0.06 mJy). We add Gaussian noise with a σ of 0.02 mJy derived from the integrated intensity map of $NH_3(1,1)$ and convolve the synthetic profile with the 6″ Gaussian beam. We uniformly sample the parameter space of $R_{\rm flat}$ between 2000 and 10,000 au and the exponent p between 2.0 and 6.0. Arzoumanian et al. (2019) defined the contrast C^0 of a profile as

$$C^0 = \frac{I_{\rm peak} - I_{\rm bkg}}{I_{\rm bkg}}, \tag{D1}$$

where $I_{\rm peak}$ and $I_{\rm bkg}$ are the peak and background intensity of the profile, respectively. For the correlation plot in Figure 9, we exclude all perpendicular profiles that are at the tips of the filaments. For the remaining filaments, the contrast ranges between 8 and 60. Values larger than 2.0 are commonly considered high-contrast profiles. To test the same contrast regime, we set the peak intensity A between 0.54 and 3.66 mJy. In total, we sample 4000 unique parameter sets and fit each of them for 20 different noise seeds.

Input parameter guesses are based on the fit of a Gaussian to the innermost part of each profile, where (1) the Gaussian amplitude is used as the initial guess of the Plummer A parameter and (2) the Gaussian σ divided by 2 is used as an initial guess for $R_{\rm flat}$. For the exponent, we set the initial guess to 3 (the mean of the parameter space). We employ the same fitting range as for the profile fitting performed in the paper, i.e., we fit the profile between −6000 and 15,000 au. Hence, we cut off one shoulder of the profile and include the major part of the shoulder on the other side. We convert the fitting parameter A to central density using Equation (7).

We perform additional masking to remove poor fit results on a profile-by-profile basis. We remove all profiles with an associated uncertainty >1500 au in flattening radius $R_{\rm flat}$, >1.2 in the exponent p, and $>3.4 \times 10^6$ (cm^{-3}) in central density n_0. These are three times the maximum of the uncertainty of each parameter in the fit of the observational profiles.

In Figure 14, we show the relation between each fitted parameter and the corresponding input parameter. For all parameters, the fitted values recover the input values within the uncertainties. The uncertainties increase toward larger values of $R_{\rm flat}$ and steeper profiles. This mainly has to do with the profiles becoming wider and the fitting range cutting off before the shoulder is reached. However, the mean of all fits recovers the input values.

ORCID iDs

Anika Schmiedeke https://orcid.org/0000-0002-1730-8832
Jaime E. Pineda https://orcid.org/0000-0002-3972-1978
Paola Caselli https://orcid.org/0000-0003-1481-7911
Héctor G. Arce https://orcid.org/0000-0001-5653-7817
Gary A. Fuller https://orcid.org/0000-0001-8509-1818
Alyssa A. Goodman https://orcid.org/0000-0003-1312-0477
María José Maureira https://orcid.org/0000-0002-7026-8163
Stella S. R. Offner https://orcid.org/0000-0003-1252-9916
Dominique Segura-Cox https://orcid.org/0000-0003-3172-6763
Daniel Seifried https://orcid.org/0000-0002-0368-9160

References

André, P., Di Francesco, J., Ward-Thompson, D., et al. 2014, in Protostars and Planets VI, ed. H. Beuther et al. (Tucson, AZ: Univ. Arizona Press), 27
André, P., Men'shchikov, A., Bontemps, S., et al. 2010, A&A, 518, L102
Arzoumanian, D., André, P., Didelon, P., et al. 2011, A&A, 529, L6
Arzoumanian, D., André, P., Könyves, V., et al. 2019, A&A, 621, A42
Arzoumanian, D., Shimajiri, Y., Inutsuka, S.-i., Inoue, T., & Tachihara, K. 2018, PASJ, 70, 96
Astropy Collaboration, Price-Whelan, A. M., Sipőcz, B. M., et al. 2018, AJ, 156, 123
Astropy Collaboration, Robitaille, T. P., Tollerud, E. J., et al. 2013, A&A, 558, A33
Bergin, E. A., & Tafalla, M. 2007, ARA&A, 45, 339
Caselli, P., Benson, P. J., Myers, P. C., & Tafalla, M. 2002, ApJ, 572, 238
Chapin, E. L., Berry, D. S., Gibb, A. G., et al. 2013, MNRAS, 430, 2545
Chapman, N. L., Goldsmith, P. F., Pineda, J. L., et al. 2011, ApJ, 741, 21
Chen, M. C.-Y., Francesco, J. D., Rosolowsky, E., et al. 2020, ApJ, 891, 84
Clarke, S. D., Williams, G. M., Ibáñez-Mejía, J. C., & Walch, S. 2019, MNRAS, 484, 4024
Coudé, S., Bastien, P., Houde, M., et al. 2019, ApJ, 877, 88

Crapsi, A., Caselli, P., Walmsley, C. M., et al. 2005, ApJ, 619, 379
di Francesco, J., Evans, N. J. I., Caselli, P., et al. 2007, in Protostars and Planets V, ed. B. Reipurth, D. Jewitt, & K. Keil (Tucson, AZ: Univ. Arizona Press), 17
Fernández-López, M., Arce, H. G., Looney, L., et al. 2014, ApJL, 790, L19
Fiege, J. D., & Pudritz, R. E. 2000a, MNRAS, 311, 85
Fiege, J. D., & Pudritz, R. E. 2000b, MNRAS, 311, 105
Friesen, R. K., Di Francesco, J., Shirley, Y. L., & Myers, P. C. 2009, ApJ, 697, 1457
Friesen, R. K., Pineda, J. E., co-PIs, et al. 2017, ApJ, 843, 63
Fuller, G. A., & Myers, P. C. 1992, ApJ, 384, 523
Fuller, G. A., Myers, P. C., Welch, W. J., et al. 1991, ApJ, 376, 135
Ginsburg, A., & Mirocha, J. 2011, PySpecKit: Python Spectroscopic Toolkit, Astrophysics Source Code Library, ascl:1109.001
Goodman, A. A., Barranco, J. A., Wilner, D. J., & Heyer, M. H. 1998, ApJ, 504, 223
Hacar, A., Alves, J., Tafalla, M., & Goicoechea, J. R. 2017, A&A, 602, L2
Hacar, A., & Tafalla, M. 2011, A&A, 533, A34
Hacar, A., Tafalla, M., Forbrich, J., et al. 2018, A&A, 610, A77
Hacar, A., Tafalla, M., Kauffmann, J., & Kovács, A. 2013, A&A, 554, A55
Hanawa, T., Kudoh, T., & Tomisaka, K. 2017, ApJ, 848, 2
Hanawa, T., Kudoh, T., & Tomisaka, K. 2019, ApJ, 881, 97
Heigl, S., Gritschneder, M., & Burkert, A. 2020, MNRAS, 495, 758
Henshaw, J. D., Caselli, P., Fontani, F., et al. 2013, MNRAS, 428, 3425
Hildebrand, R. H. 1983, QJRAS, 24, 267
Ho, P. T. P., & Townes, C. H. 1983, ARA&A, 21, 239
Holland, W. S., Bintley, D., Chapin, E. L., et al. 2013, MNRAS, 430, 2513
Kainulainen, J., Hacar, A., Alves, J., et al. 2016, A&A, 586, A27
Kauffmann, J., Bertoldi, F., Bourke, T. L., Evans, N. J. I., & Lee, C. W. 2008, A&A, 487, 993
Kirk, H., Klassen, M., Pudritz, R., & Pillsworth, S. 2015, ApJ, 802, 75
Koch, E. W., & Rosolowsky, E. W. 2015, MNRAS, 452, 3435
Könyves, V., André, P., Men'shchikov, A., et al. 2015, A&A, 584, A91
Larson, R. B. 1981, MNRAS, 194, 809
Liu, J., Qiu, K., Berry, D., et al. 2019, ApJ, 877, 43
Monsch, K., Pineda, J. E., Liu, H. B., et al. 2018, ApJ, 861, 77
Newville, M., Stensitzki, T., Allen, D. B., et al. 2016, Lmfit: Non-Linear Least-Square Minimization and Curve-Fitting for Python, Astrophysics Source Code Library, ascl:1606.014
Ossenkopf, V., & Henning, T. 1994, A&A, 291, 943
Ostriker, J. 1964, ApJ, 140, 1056
Palmeirim, P., André, P., Kirk, J., et al. 2013, A&A, 550, A38
Panopoulou, G. V., Psaradaki, I., Skalidis, R., Tassis, K., & Andrews, J. J. 2017, MNRAS, 466, 2529
Panopoulou, G. V., Tassis, K., Goldsmith, P. F., & Heyer, M. H. 2014, MNRAS, 444, 2507
Pattle, K., Lai, S.-P., Di Francesco, J., et al. 2021, ApJ, 907, 88
Pezzuto, S., Benedettini, M., Di Francesco, J., et al. 2021, A&A, 645, A55
Pezzuto, S., Elia, D., Schisano, E., et al. 2012, A&A, 547, A54
Pineda, J. E., Goodman, A. A., Arce, H. G., et al. 2010, ApJL, 712, L116
Pineda, J. E., Goodman, A. A., Arce, H. G., et al. 2011, ApJL, 739, L2
Pineda, J. E., Offner, S. S. R., Parker, R. J., et al. 2015, Natur, 518, 213
Robitaille, T., & Bressert, E. 2012, APLpy: Astronomical Plotting Library in Python, Astrophysics Source Code Library, ascl:1208.017
Robitaille, T., Ginsburg, A., Beaumont, C., Leroy, A., & Rosolowsky, E. 2016, Spectral-cube: Read and Analyze Astrophysical Spectral Data Cubes, Astrophysics Source Code Library, ascl:1609.017
Robotham, A. S. G., & Obreschkow, D. 2015, PASA, 32, e033
Rosolowsky, E. W., Pineda, J. E., Kauffmann, J., & Goodman, A. A. 2008, ApJ, 679, 1338
Seifried, D., & Walch, S. 2015, MNRAS, 452, 2410
Smith, R. J., Glover, S. C. O., & Klessen, R. S. 2014, MNRAS, 445, 2900
Smith, R. J., Glover, S. C. O., Klessen, R. S., & Fuller, G. A. 2016, MNRAS, 455, 3640
Stodólkiewicz, J. S. 1963, AcA, 13, 30
Stutz, A. M., & Kainulainen, J. 2015, A&A, 577, L6
Stutzki, J., Jackson, J. M., Olberg, M., Barrett, A. H., & Winnewisser, G. 1984, A&A, 139, 258
Sugitani, K., Nakamura, F., Watanabe, M., et al. 2011, ApJ, 734, 63
Suri, S., Sánchez-Monge, Á, Schilke, P., et al. 2019, A&A, 623, A142
Tomisaka, K. 2014, ApJ, 785, 24
Van Der Walt, S., Colbert, S. C., & Varoquaux, G. 2011, CSE, 13, 22
Ward-Thompson, D., André, P., Crutcher, R., et al. 2007, in Protostars and Planets V, ed. B. Reipurth, D. Jewitt, & K. Keil (Tucson, AZ: Univ. Arizona Press), 33
Zucker, C., & Chen, H. H.-H. 2018, ApJ, 864, 152
Zucker, C., Schlafly, E. F., Speagle, J. S., et al. 2018, ApJ, 869, 83